Laser Diodes Power Scaling Techniques

BY

MATTIA CAFFA
B.S, Politecnico di Torino, Turin, Italy, 2018

THESIS

Submitted as partial fulfillment of the requirements
for the degree of Master of Science in Electrical and Computer Engineering
in the Graduate College of the
University of Illinois at Chicago, 2020

Chicago, Illinois

Defense Committee:

Piergiorgio L. E. Uslenghi, Chair and Co-Advisor
Danilo Erricolo
Guido Perrone, Politecnico di Torino, Co-Advisor

ACKNOWLEDGMENTS

I want to thank my family who allowed me to have an amazing experience in Chicago during this year.

I would like to thank my advisor Guido Perrone and the people from OpiPhotonics who have shared their experiences and have given me the opportunity to work in their research group.

Finally, I would like to thank Silvia who stands by me, supports me everyday and without whom these last five years would have not been the same.

MC

TABLE OF CONTENTS

TABLE OF CONTENTS (continued)

CHAPTER **PAGE**

LIST OF TABLES

LIST OF FIGURES

LIST OF ABBREVIATIONS

AOM	Acousto-Optic Modulator
BFL	Back Focal Length
CBC	Coherent Beam Combining
CCD	Charge Couple Device
CT	Central Thickness
DAQ	Data Acquisition
EFL	Effective Focal Length
EOM	Electro-Optic Modulator
FFT	Fast Fourier Transform
FPGA	Field Programmable Gate Array
MFD	Mode Field Diameter
MOPA	Master Oscillator Power Amplifier
LOCSET	Locking of Optical Coherence by Single Detector Electronics Frequency Tagging
PM	Polarization Maintaining
[SBC	Spectral Beam Combining
SPGD	Stochastic Parallel Gradient Descent

LIST OF ABBREVIATIONS (continued)

TE	Transverse Electric
TM	Transverse Magnetic

SUMMARY

In this work the problem of laser power scaling and brightness improvement is addressed. The limits that the development of single laser devices (both semiconductor lasers and fiber lasers) has reached and hardly can surpass are discussed and an overview on the different techniques to combine multiple lasers into a single beam with greater power and quality is presented.

Among these techniques active combining stand out, for the promising results that have already been obtained and its importance in future research,and thus it has been investigated in detail. To this purpose a MOPA system seeded with a fiber laser has been numerically simulated using Matlab and an active phase correction algorithm has been validated.

In the last part of the thesis, preliminary experiment results on spectral beam combining - another promising power scaling technique- are described. In particular, locking and combining at different wavelengths, using as feedback the first order of a blazed diffraction grating, have been demonstrated with multiple diodes.

CHAPTER 1

INTRODUCTION

High power lasers have found successful application in different fields, such as: in industrial material processing, in medical treatments and in military applications. Power scaling techniques have been a popular topic in the last decades and their relevance has increased with time since the single device scaling limit has almost been reached.

In this work, different ways of dealing with the increasing demand of power while maintaining good quality of the laser beam are discussed. A method to coherently combine multiple beams has been numerically simulated to see if the expected theoretical results can be obtained in realistic implementation and an algorithm to actively correct the phase relation has been validated. Also, a spectral beam combining set-up has been experimentally tested and the results are presented.

1.1 Thesis Structure

In Chapter 2 an overview on high power laser's state of the art and power scaling techniques based on beam combining are discussed.

Chapter 3 shows how the simulation of a Master Oscillator Power Amplifier configuration for coherent combining has been performed and what results it can achieve.

In Chapter 4 the algorithm to actively correct the phase of the beams in the previously described system is presented and validated.

Chapter 5 describes the experimental implementation and the results obtained with a spectral beam combining technique.

Chapter 6 summarizes the thesis discussion and the results that have been obtained.

CHAPTER 2

HIGH POWER LASERS

In this chapter a review on high power laser technologies is presented. In the first part, the power scaling of single devices and its limitations are discussed. The second part focuses instead on combining techniques. Before that, a specification on what beam quality means is needed.

2.1 Beam Quality Parameters

When the quality of a beam needs to be evaluated, certain parameters have to be considered. One of these is the M^2 factor, which is a term of comparison between the shape of the beam and shape of a Gaussian beam and is defined as

$$M^2 = \frac{\pi w_0 \theta_d}{\lambda} \tag{2.1}$$

where θ_d is the divergence angle of the beam and w_0 is the beam radius (deeper analysis on Gaussian beam is presented in Section 3.2). For an ideal Gaussian beam with flat phase front (diffraction limited) at the waist the divergence angle is such that $M^2 = 1$. This quantity therefore represents how much the beam differs from an ideal Gaussian one and should be as close as possible to 1 (lower values cannot be achieved). A beam with a lower M^2 than another "*correspond with a tighter focus, a more efficient use of the power within the beam, and a higher potential effective power of the laser*" [1].

Another parameter that is used as an alternative and is related to the M^2 factor is the beam parameter product (BPP)

$$BPP = \frac{M^2}{\lambda} \tag{2.2}$$

Finally, when quality and power need to be considered at the same time, a concept similar to power density is introduced: the brightness (or radiance) of the diodes, defined as the power delivered on unit area and solid angle [2]

$$B = \frac{P}{A\Omega} = \frac{P}{M_x^2 M_y^2 \lambda^2} \tag{2.3}$$

Where M_x^2 and M_y^2 are the M^2 factor in the horizontal and vertical directions. We can see that this parameter is proportional to the power and inversely proportional to the quality of the beam.

2.2 State of the Art of Single Device Technology

High power lasers are required in industrial applications such as different sort of material processing, military applications, remote sensing and other activities. Over the years the power of single devices has been scaled while keeping the quality of the beams as good as possible.

A single mode diode can reach up to 1 W power [3] with diffraction limited brightness ($M_x^2 = 1, M_y^2 = 1$).

Multimode diodes have been exploited to scale the power of single devices: at first broad area lasers have been introduced reaching 7 W of power but with a reduced brightness ($M_x^2 =$

$1, M_y^2 = 6$)[4]. This problem has been solved with the development of tapered laser diodes which can achieve an optical power of 12 W and with $M_x^2 = 1$, $M_y^2 = 1.2$ [5].

The maximum power that a diode can achieve has however reached a limit imposed by catastrophic optical damages [6]. This phenomenon verifies when the power density on the diode junction is too high and it absorbs too much energy, leading to facet materials melting and therefore, device failure. A bigger volume to have a more distributed power would lead to an M^2 increase. Therefore, further improvements of this technology are not to be expected if not with a complete innovative design and/or a discover of new material with suitable properties.

Higher power and brightness have been achieved with fiber lasers which are based on a fiber gain medium pumped from another source (namely multimode diodes array or solid-state pump). Indeed, with such a device the kW range, with almost ideal beam quality, has been reached. In 2017 a German research has obtained a single mode fiber laser, seeded with a 10 W diode, with an output power of 4.3 kW and a factor $M^2 \approx 1.3$ in both directions [7].

Also, power scaling of fiber lasers is limited by the onset of non-linear phenomena such as: stimulated Brillouin scattering and the rise of transverse modes instability due to heat load. Nevertheless, the German research group claims their system could achieve improved performance with a greater pump power. A further scaling is therefore limited, also in this case, from diode and solid state technology.

2.3 Beam Combining

The only way to achieve greater power is to combine multiple lasers in a single beam. Different techniques of laser combining have been studied. When considering the trade-off between power and quality there are two possible choices: incoherent or coherent beam combining.

In the former case, no relation between the phases of different beams must be established and for this reason it is easier to be achieved. In the latter instead, the channels must establish mutual phase coherence and this relation must be kept for the whole duration of the operations.

Coherent combining requires accurate phase control and has usually a lower scalability (in the number of channels) with respect to the incoherent one and this means lower power achievable. However coherently combined beams usually have a narrower spectral occupation which can be crucial for certain applications.

2.4 Incoherent Combining

Incoherent combining is the easiest way of increasing the power of multiple devices. There are three possible ways of achieving it: spatial, polarization and wavelength combining.

2.4.1 Spatial Beam Combining

Spatial combining, also called spatial overlapping, is a technique that consists in combining the beams positioning them near to each other into linear or multidimensional array. Pointing the beam in the same direction will overlap them in the far field, giving rise to a single beam. This is a simple technique, thus very appealing. However, while the power is scaled as N (number of beams) also the area on which it is distributed is increased. In this case Equation 2.3 becomes [8]

$$B = \frac{NP}{NA\Omega} \tag{2.4}$$

and the brightness will be in the best case the same one of a single channel. This result can also be seen as the increase by a factor of N of the M^2 parameter.

2.4.2 Polarization Beam Combining

Polarization combining or multiplexing consists in a system which sum two orthogonally polarized beams into a single one. This operation, which requires two linearly polarized beam can be done rotating one beam by 90^o with a half-waveplate and then combining the beams with polarizing beam splitter or birefringent crystal.

The polarization multiplexing technique maintains the quality of the beam unchanged but permits to scale the power by a factor of 2 only.

2.4.3 Spectral Beam Combining

In contrast with the previously mentioned techniques, spectral beam combining (SBC), or wavelength multiplexing, permits scaling of both power and brightness.

The idea is to combine beams with different wavelengths along the same optical path. The wavelengths can be combined all together exploiting a prism or a grating, or in multiple stages in pairs by means of dichroic mirrors. The former case imposes more restrictive constraints regarding wavelength stabilization and sensibility of the beam to temperature and current fluctuations. In the latter, these requirements are weaker, but N-1 mirrors are needed to combine N wavelengths as shown in Figure 1.

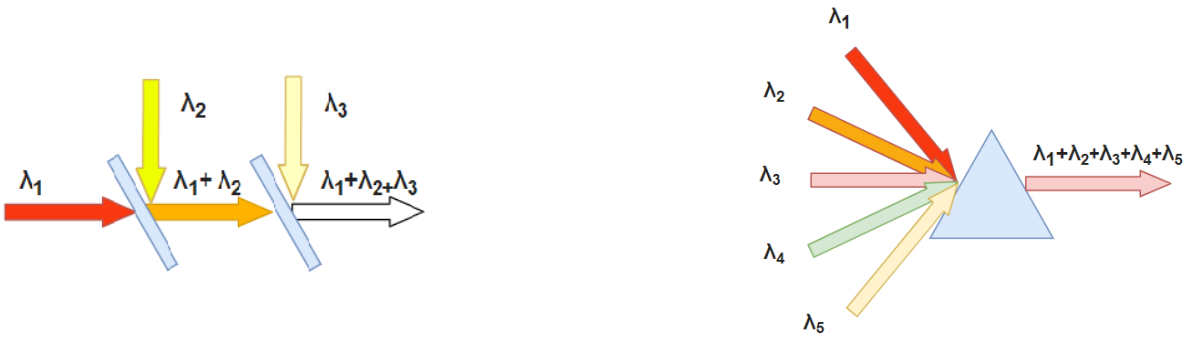

(a) Dichroic mirrors (b) Prism

Figure 1: Wavelength combining with different optical elements

In both cases, since each beam is distinguishable for its unique wavelength the combined beam will emerge on the output of the diffractive element as a single beam with the same quality of the starting ones. Therefore, if two diffraction limited beams are combined, the result is a diffraction limited beam with increased power. In this way the radiance equation becomes

$$B = \frac{NP}{A\Omega} \tag{2.5}$$

and it is possible to see that is increased by a factor of N with respect to that of a single beam. The only drawback of the SBC method is that, since different wavelengths are combined together, the output will have a wider spectral occupation. For example,exploiting the SBC technique, 8 fibers have been combined for a total output power of 10.8 kW, although with a not optimal beam quality due to degradations in high power operations[9]; in another experiment, a 2.3 kW beam with $M^2 = 1.5$ has been demonstrated combining four channels in [10].

2.5 Coherent Beam Combining

In certain applications, such as pumping of particular materials very narrow spectral line width and high brightness are required. For this scenarios coherent beam combining (CBC) is exploited.

With this combination technique the coherent beams are spatially overlapped with a tiled aperture (side by side) or with a filled aperture(**??**) in which the beams are combined with a diffractive element (differently from SBC, the beams must have the same wavelength and have polarization).

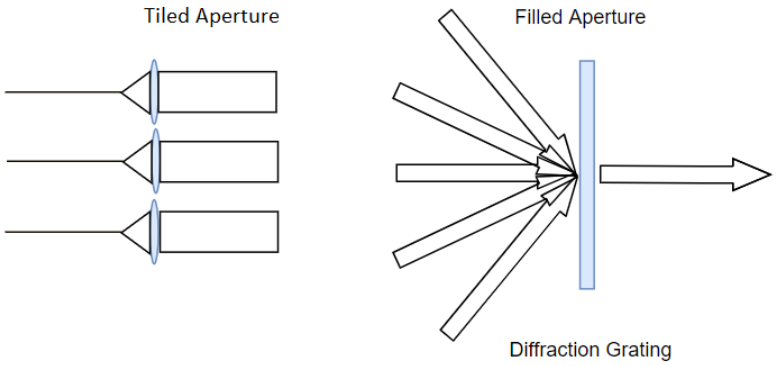

Figure 2: Aperture types for CBC

Tiling the beams together is easier but the interference pattern caused from the spacing between the channels (filling factor) will give rise to sidelobes in the farfield and the total

power will be spread out among the various peak. A filled aperture is not affected from this problem but requires a more precise design and a diffractive element that can withstand the power of all the beams focused on a small area. For very high power systems it is not always possible to have an element with such properties.

To increase the power in the CBC method, more lasers are added in the array increasing the emitting aperture size and a combined beam with the spot size of a single one can be obtained. The effect of constructive interference leads to on axis peak intensity scaling proportional to N^2.

As previously mentioned, mutual coherence between the beams must be established and, in order to achieve it, a very precise phase control is needed. Usually, controlling the phase is more complicated than controlling the wavelength, therefore SBC is preferred when the requirements on the spectral occupation are not too much demanding.

The phase coherence in CBC is established and maintained either with a passive or active feedback. Passive methods are based on external cavity resonators such as Talbot cavities, interferometers, or Fourier cavities [11], which can self-adjust the phase of the beams. Even if good results have been obtained with this method, as for example a combined power of 6.7 W from two 4 W diodes (82% efficiency) [12] and 710 W for a passively locked master oscillator power amplifier (MOPA) configuration seeded with a fiber laser [13], the combining efficiency tends to decrease rapidly with an increasing number of channels (N should stay lower than 8).

Active combining is based on electronics control of the phase relation between the beams. Usually the previously mentioned MOPA configuration is exploited. A master oscillator (it

should be a narrow line, low power laser: either a diode or a fiber laser) is used as seed to feed multiple channels and, since the beams come from the same seed, they will be mutually coherent. Subsequently they are amplified and spatially combined. The phase relation must then be adjusted to maximize the output beam. With active CBC method the incredible result of a 105.5 kW with a beam quality of 2.9x diffraction limit has been demonstrated for a bulk laser array [14], while a 4 kW laser with 1.25x diffraction limit quality has been shown in [15] using a fiber array.

The most common methods to actively adjust the phase in the MOPA configuration:

- Heterodyne phase shifting;
- Stochastic parallel gradient descent (SPGD) algorithm;
- LOCSET (Locking of Optical Coherence by Single Detector Electronics Frequency Tagging) method.

2.5.1 Heterodyne phase shifting

The Heterodyne phase shifting set up is reported in Figure 3: the seed is split in multiple channels (N+1). The N channels pass through an electro-optic modulator (analyzed in depth in Section 3.1) which can shift the phase of the channel with an applied voltage; then they are amplified, collimated and sent to a partially reflecting mirror (small power reflected). The (N+1)th channel instead passes through an acousto-optic modulator (AOM), which allows shifting the frequency of the beam. It is then collimated with a beam width greater than the tiled combined beams of the N channels and sent on the same reflecting mirror. N photodetectors

receive the reflected interference of the reference beam and the amplified ones. The beat notes absorbed on the detector contain the information of the phase difference of each channel with respect to the reference one (the N+1) and the control electronics is designed to minimize this difference. The control electronics for a single channel correction is shown in Figure 8 of

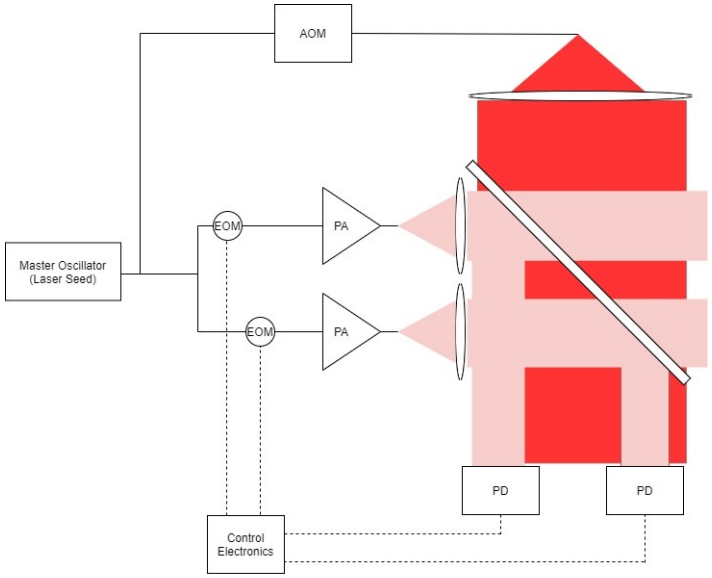

Figure 3: MOPA heterodyne architecture

[16] and consists of a sum and a difference operation (between the reference and signal arm) implemented with mixers and a logic XOR which outputs a signal, with duty cycle proportional to the phase difference, which is used to control the EOM of the corresponding channel. These operations need to be implemented for each of the N channels. To obtain the correct interference

on the photodetectors the reference beam must be perfectly aligned with the others and, when the number of channels increases, this operation becomes more complicated; however, scalability for this method is not limited. As a drawback there is no direct way to assure all the N channels are locked to each other.

2.5.2 Stochastic Parallel Gradient Descent

The active phase correction by means of SPGD algorithm is discussed in detail in Chapter 4 therefore just an overview is provided in the following.

The set-up is similar to the heterodyne techniques one but it has some improvements since the reference arm with the AOM is not needed and only one photodetecor is required. Indeed, to be sent as a feedack is not an interference between different beams but is a fraction of the combined focused light. The current of the photodetector is used to generate multiple contemporary signals to adjust the phase. In this case, the phase relation between the beams is not known and the optimization is based on the intensity of the beam. SPGD technique can be implemented easily in laboratory since an FPGA is sufficient as control electronics and it also has the advantage of being able to correct other aberration such as tilt/tip control. The main drawback is that the bandwidth of the control loop (and thus the speed of the system) is inversely proportional to the number of channels [17].

2.5.3 LOCSET Method

As well as the SPGD method, LOCSET technique requires just a single photodetector. The set-up is the same of the previous case but the control electronics system is different. LOCSET is not based on an intensity maximization algorithm but on RF demodulation. At

each channel is applied a small amplitude phase perturbation at an unique frequency called "tag". Thanks to this operation the output beam measured on the photodetector will contain the phase information needed for CBC. The photocurrent will have a contribution from each of the tagged beams. The control electronics carries out a demodulation operation for each of the channel (namely the modulation frequency is equal to the frequency of the unique tag) and integrates over time the obtained signal to generate the phase error correction one to drive to EOM. Clearly, for a large number of channels the control electronics can be very complex and expensive, but, this method has the advantage of not having bandwidth limitation as in the case of the SPGD one.

2.5.4 Comparison

In Table I a summary of pros and cons of the three methods is reported. The heterodyne phase shifting is the best choice if the number of beams to be combined is small and a simple design and implementation is one of the requirements. If the number of channels is higher, costs (increased from the AOM and the multiple photodetector) and efficiency will direct the choice on the other two methods. If multiple aberrations need to be corrected and still a simpler design is needed, then the only solution is to exploit the SPGD algorithm. If, instead, the number of channels is elevated and a good efficiency is required, LOCSET should be selected.

TABLE I: PROS AND CONS OF COHERENT COMBINING METHODS

	Heterodyne	SPGD	LOCSET
Unique Requirements	Reference Channel, AOM, N photodetectors	FPGA	High Frequency Modulation and Demodulation Electronics
Possible Correction	Piston Phase	Piston Phase, tilt/tip control and other aberration	Piston Phase
Number of Channels	No limit	8 (single detector), 48 (multiple detectors). A further increase would limit too much the bandwidth	32 demonstrated but more channels can be combined

CHAPTER 3

SIMULATION ON COHERENT COMBINING

A full simulation of a coherent beam combining system with SPGD active phase control has been performed and is discussed in this chapter. The system is composed by a master oscillator used as seed for multiple channels. Different lasers would have a random phase relation in time but, since the channels are seeded from the same laser, a phase relation between the two is guaranteed.

On each fiber is located an electro-optic modulator (EOM) needed to correct the phase relation in order to established and maintain coherence. The output beams are disposed in tiled aperture, which means they are positioned next to each other in the near field [18] and they combine together only in the far field.

The outputs are collimated and then, with a lens, they are focused onto a target where a power meter is located. A small percentage of incident power is split in part toward a CCD (charge couple device) camera to visualize the far field pattern of the combined beams and in part toward a pinhole photodetector exploiting partial reflecting mirrors.

The current generated from the photodetector is sent to control electronics which, following the stochastic parallel gradient descent (SPGD) method, will generate the voltages to drive the EOMs in the correct way.

As proof of concept and to validate the algorithm in the simulation it has been supposed that the fiber outputs are ideal Gaussian beams and that all the power is incident on the photodetector.

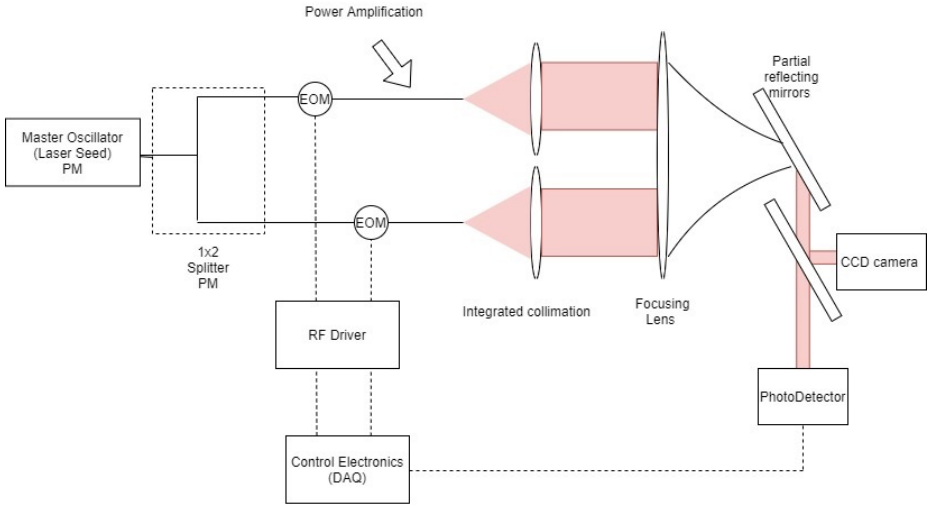

Figure 4: MOPA architecture with SPGD correction

3.1 Electro-Optic Modulators

Optical modulators are fundamental devices for different applications such as power modulation, frequency stabilization, high speed communication, active mode locking, encoding and coherent beam combining [19].

Optical modulators can be used to modulate:

- intensity
- polarization
- phase

The EOMs in the system under analysis are phase modulators. They exist both for free space or for fiber applications. Usually they are Lithium Niobate ($LiNbO_3$) waveguides whose refractive index can be changed by applying either a constant or an alternate voltage inducing a delay in the path.

The refractive index variation, as mentioned in [20] is linearly dependent on the electric field as

$$\Delta_n = \frac{1}{2}(n_e^3 r_{33})E \tag{3.1}$$

where n_e and r_{33} are, respectively,the dynamic refractive index and an intrinsic non-linear coefficient. This phenomenon, called electro-optic effect, can be exploited to tune the phase relation between different channels.

As shown in [21], commercial EOMs' phase variation depends linearly with the applied RF voltage.

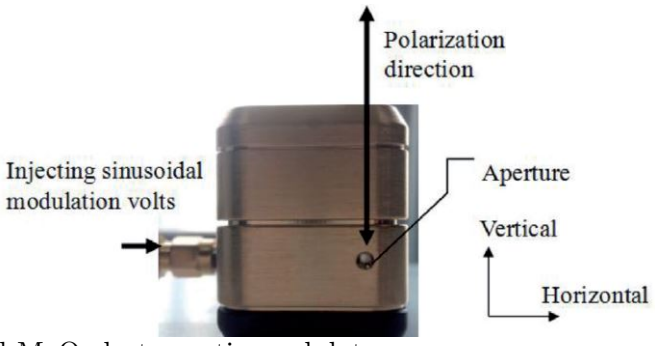

Figure 5: Commercial MgO electro-optic modulator-
Credits[Yufeng Tao[CC BY-SA 3.0 (http://creativecommons.org/licenses/by/3.0/)],IntechOpen

When the applied voltage is equal to the half drive voltage (specified on the datasheet) $V(t) = V_\pi$ then the phase shift is $\phi(t) = \pi$.

For full modulation depth (from $-\pi$ to π) a peak to peak voltage of $2V_\pi$ is required.

3.2 Fiber and Collimation

To achieve constructive interference, the outputs from the fibers must be copolarized [22]. Therefore, PM fibers should be selected [23] to maintain polarization across the whole system. Choosing a common operating wavelength $\lambda = 1550$ nm allows us to find specifications of a real fiber to be used in the simulation.

For example, a PM1550-XP from Thorlabs has the dimension reported in Table II.

The mode field diameter (MFD) is particularly relevant since it gives information about the size of the optical output of the fiber. It is defined as "*the radial position where the intensity falls to* e^{-2} *of the peak intensity* " [24].

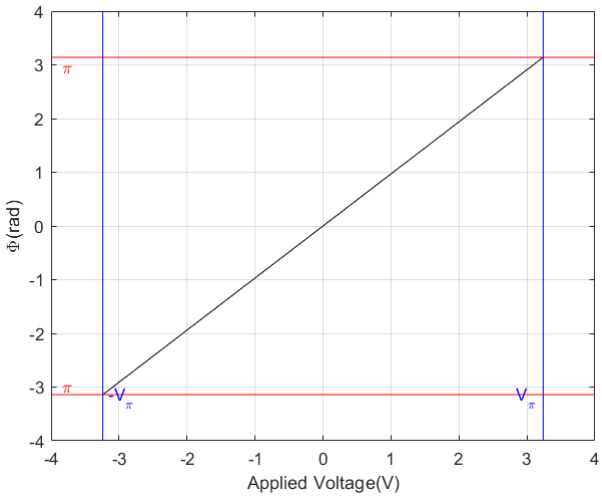

Figure 6: EOM: phase variation vs applied voltage

TABLE II: COMMERCIAL PM FIBER DIMENSION

core diameter	8.5 μm
cladding diameter	125 $\pm$ 2 μm
coating diameter	245 $\pm$ 15 μm
MFD	10.4 μm

Before focusing, beams are usually collimated in such a way their divergence is almost negligible for small distances.

Considering Gaussian beams, the half width of the beam is a function of z and can be expressed as

$$w^2(z) = w_0^2(1 + \frac{z}{z_0})^2 \tag{3.2}$$

where w_0 is the minimum radius of the beam (measured where the field intensity is $\frac{1}{e}$ of the peak) and is called beam waist and z_0 is the so called Rayleigh length [25]. This is the distance at which the width of the beam is a factor $\sqrt{2}$ larger than the initial beam waist and it can be computed as

$$z_0 = \frac{\pi w_0^2}{\lambda} \tag{3.3}$$

Since we are considering Gaussian beam outputs, it can be assumed that $MFD = 2w_0$.

From Equation 3.2 it can be seen that the width of the beam increases, and thus diverges, faster with z if associated with a smaller beam waist.

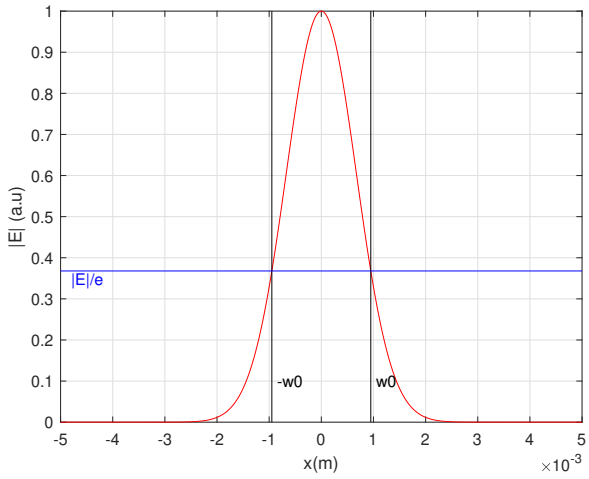

Figure 7: Profile of the field of a single beam after collimation

A collimating lens, to work properly, needs to increase the waist of the input beam. Collimation can be either done with integrated connectors or in air by means of lenses. In this work the former option has been selected and the new waist diameter can be computed as stated in [26] as

$$d \approx 4\lambda \frac{fc}{\pi MFD} \tag{3.4}$$

where f_c is the focal length of the collimator.

For example, when a PAF2P-A10C connector, which has an integrated lens with effective focal length(EFL) 10 mm and MFD input of 10.4 um (compatible with the chosen fiber), is selected, the new beam waist radius for each of the beams will be $w_0 = \frac{d}{2} \approx 0.95$ mm.

The centroids of the beams will not be overlapped due to mechanical elements. The profile of the field after collimation (in the case of 2 channel) will be the one in Figure 8.

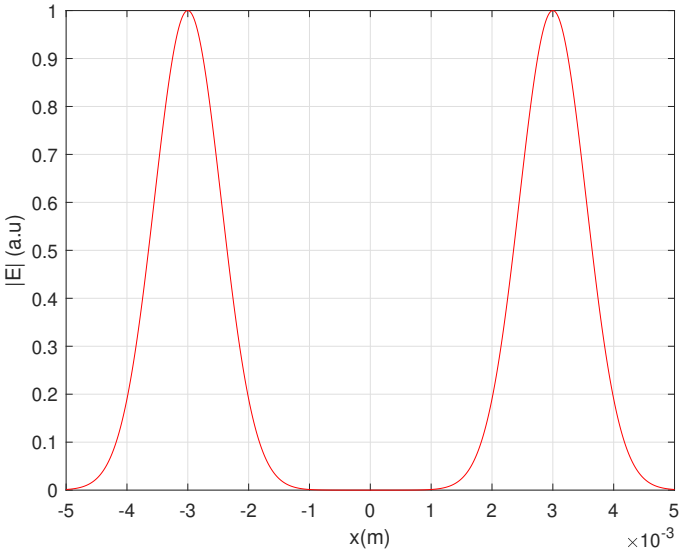

Figure 8: Collimated beams

3.3 Ideal Propagation of Gaussian Beams

The collimated beams are then propagated in air at the distance z where the focusing lens is located. Propagation of Gaussian beams along the z axis is well known [27] and is

$$E(x,\ y,\ z) = E_0 \frac{w_0}{w(z)} e^{\left(-\frac{r(x,y)^2}{w(z)^2}\right)} e^{\left(-j(kz - \tan^{-1}(\frac{z}{z_0}))\right)} \left(e^{(-\frac{jkr^2}{2R(z)})}\right) \tag{3.5}$$

where

- $r = x^2 + y^2$ is the radius;
- $R(z) = z + \frac{z_0^2}{z}$ is the radius of curvature of the phase front;

- $E_0 \frac{w_0}{w(z)} \exp\Big(- \frac{r(x,y)^2}{w(z)^2}\Big)$ is an attenuation term;
- $\exp\Big(- j(kz - \tan^{-1}(\frac{z}{z_0})\Big)$ is a phase factor;
- $(\exp(-\frac{jkr^2}{2R(z)})$ is a radial phase factor.

3.4 Focusing lens

After propagation, the beams need to be focused onto the chosen target with a proper lens.

The lens introduces a phase variation, $\Phi(x, y)$, dependent on the radius, r(x,y), and on the structure of the lens.

In [28] it is shown how to derive the phase change

$$\Phi(x, y) = kn\Delta_{\phi_{tot}} + k[CT - \Delta_{\phi_{tot}}] \tag{3.6}$$

with CT being the central thickness (at x=0,y=0) of the lens.

Dividing the lens in three parts, namely the two curvatures ones and the central one of the lens, the total phase change is

$$\Delta_{\phi_{tot}}(x,\ y) = \Delta_{\phi_1}(x,\ y) + \Delta_{\phi_2}(x,\ y) + \Delta_{\phi_3}(x,\ y) \tag{3.7}$$

While $\Delta\phi_2$ is usually given by the supplier and is constant with x and y, Δ_{ϕ_1} and Δ_{ϕ_3} need to be obtained from the specifications.

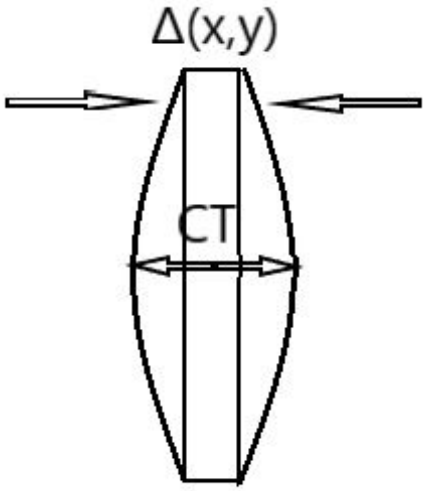

(a) Lens scheme

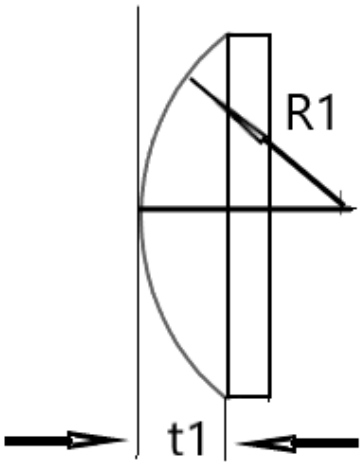

(b) Plano-convex lens

Following Figure 9b Equation 3.8 can be derived geometrically as

$$\Delta_{\phi_1} = t_1 - (R_1 - \sqrt{R_1^2 - x^2 - y^2}) \tag{3.8}$$

Δ_{ϕ_3} can be obtained in a similar way.

Once the phase function is known, it is straightforward to compute the field after the lens

$$E_{after}(x, y) = E_{before}(x, y) exp(j\Phi(x, y)) \tag{3.9}$$

The phase change will make light rays converge toward a point called the focus. In this point the combined beam has minimum width and therefore higher power density. The target will be then located at the focus distance.

To focus the beam, the lens has been chosen to be a plano-convex lens (without the second curvature part: Δ_3).

The values of the dimensions for the simulation have been taken from 1550 nm commercial lenses supplied by Edmund Optics [29].

TABLE III: LENS DIMENSION

Diameter	5 mm
EFL	15 mm
BFL	13.94 mm
refractive index(n) @1550 nm	$\tilde{1}.50$
Radius R1	7.75 mm
CT	1.20 mm
t1	0.4 mm

As first trial, a lens with the characteristics of Table III been has been chosen.

3.5 Propagation after lens

The action of the lens has changed the beam width and the divergence relation of the output. Therefore, to propagate the beam toward the target, Equation 3.5 is not suitable. In this case the theory of angular spectrum should be exploited [28].

When a complex field E(x,y,0) is incident on a transverse plane(x,y) it is possible to compute the field at distance z, i.e. E(x,y,z), mapping the field from the spatial to the spatial frequencies domain.

The field in z=0 has a 2-D Fourier transform

$$F(f_x,\ \ f_y,\ \ 0) = \int_{\infty}^{\infty}\int_{\infty}^{\infty} E(x,y,0)e^{[-j2\pi(f_x x+f_y y)]}dxdy \tag{3.10}$$

The function $\exp[-j2\pi(f_x x + f_y y)]$ can be also seen as a plane wave travelling with cosine directions

$$\theta = \lambda f_x, \qquad \gamma = \lambda, f_y \qquad \alpha = \sqrt{1-(\lambda f_x)^2-(\lambda f_y)^2} \tag{3.11}$$

following this notation Equation 3.10 can be written as

$$F(\alpha\lambda,\beta\lambda,0) = \int_{\infty}^{\infty}\int_{\infty}^{\infty} E(x,y,0)\exp[-j2\pi(\frac{\theta}{\lambda}+\frac{\gamma}{\lambda})]d\frac{\theta}{\lambda}d\frac{\gamma}{\lambda} \tag{3.12}$$

where $F(\theta\lambda,\gamma\lambda,0)$ is called angular spectrum of E(x,y,0).

Knowing the relationship between $F(\theta\lambda, \gamma\lambda, 0)$ and $F(\theta\lambda, \gamma\lambda, z)$ will allow us to find also E(x,y,z).

Indeed, the field at z is the inverse Fourier transform of the angular spectrum evaluated at same point

$$E(x, y, z) = \int_{\infty}^{\infty} \int_{\infty}^{\infty} F(\theta\lambda, \gamma\lambda, z) \exp\left[-j2\pi(\frac{\theta}{\lambda} + \frac{\gamma}{\lambda})\right] dxdy \tag{3.13}$$

It can be proved that in order to guarantee E(x,y,z) is a solution of Helmotz equation a sufficient condition is to have

$$F(\theta\lambda, \gamma\lambda, z) = F(\theta\lambda, \gamma\lambda, z) \exp\left(\frac{j2\pi}{\lambda}\sqrt{1 - (\theta)^2 - (\gamma)^2}z\right) \tag{3.14}$$

Finally, substituting Equation 3.14 in Equation 3.13 and going back to frequency notation, the propagated field is

$$E(x, y, z) = \int_{\infty}^{\infty} \int_{\infty}^{\infty} F(f_x, f_y, 0) \exp\left[-j2\pi\left(\sqrt{1 - (\lambda f_x)^2 - (\lambda f_y)^2}\right)z\right] \exp\left[-j2\pi(f_x x + f_y y)\right] dxdy \tag{3.15}$$

Summarizing the steps to be followed are:

- Compute the 2D Fourier transform of the initial field $E(x, y, 0) \rightarrow F(f_x, f_y, 0)$
- Propagate the angular spectrum $F(f_x, f_y, 0)$ at distance z in the spatial frequency domain by means of the transfer function $\rightarrow \exp\left[-j2\pi(f_x x + f_y y)\right]$
- Compute the 2D inverse Fourier transform to go back to spatial domain and find E(x,y,z).

Clearly all these steps require multiple transforms and they cannot be carried out analytically. Numerical methods such as Fast Fourier Transform (FFT) are required.

FFTs can be computed with the built-in functions of Matlab or Python although the correct parameters need to be chosen in order to avoid numerical errors. The FFT algorithm samples the selected function in a certain number of points (NFFT) in a selected range (W_x). The function will be supposed to be defined in $\frac{W_x}{2} < x < \frac{W_x}{2}$. The FFT performs the following operations (Orta 2019, Lecture Notes on Passive Optical Component, Politecnico di Torino).

$$x(n) = \frac{1}{NFFT} \sum_{k=1}^{NFFT} X(k) \exp(j2\pi(k-1)(\frac{n-1}{NFFT} \qquad 1 \leq n \leq NFFT \tag{3.16}$$

$$X(k) = \frac{1}{NFFT} \sum_{k=1}^{NFFT} x(n) \exp(-j2\pi(k-1)(\frac{n-1}{NFFT} \qquad 1 \leq k \leq NFFT \tag{3.17}$$

With $NFFT = 2^M$ and $N = \frac{NFFT}{2}$ we can define the sampling points along a direction (x or y) as

$$x_v = (-N : N-1)\frac{W_x}{NFFT} \tag{3.18}$$

and the corresponding spectral variable as

$$f_x = \frac{(-N : N-1)}{W_x} \tag{3.19}$$

With these definitions the 2D Fourier transform will be

$$f(x_v, y_v) = fft2\Big(F(f_x, f_y)\Big)\frac{1}{W_x W_y} \tag{3.20}$$

$$F(f_x, f_y) = ifft2\Big(f(x_v, y_v)\Big)W_x W_y \tag{3.21}$$

One more detail need to be specified: the provided routine uses positive indices in such a way that the first frequency component is in the first array position. We need instead to have the array starting from negative frequencies and this can be obtained by means of the function ffshift and the full lines for the transforms become

$$f(x_v, y_v) = fftshift(fft2\Big(fftshift(G(f_x, f_y)\Big)\frac{1}{W_x W_y} \tag{3.22}$$

$$F(x_v, y_v) = fftshift(ifft2\Big(fftshift(g(x_v, y_v))\Big)W_x W_y \tag{3.23}$$

Focusing on the parameters:

- If NFFT is too low the resolution will suffer, especially if the function has fast variations.
- If NFFT is too high computation time increases drastically.
- W_x must be chosen in such a way that no important information are lost. This means only negligible part of the function must stay outside the selected space window.

- Since the spacing of the samples will be $\Delta_x = W_x/N$, if W_x is too big then the resolution is reduced again (and requires an increase of NFFT).

The right trade-off between parameters need to be found with respect to the objective we want to achieve, being aware some errors will be always introduced since it is a numerical algorithm.

3.6 On Target Field

The field is propagated by means of the Fourier spectrum to a distance equal to the focal length. In this point, the width of the combined beam is minimum and therefore the power density is the highest.

The target is a photodetector with a pinhole which is a common device used for intensity maximization [30]. The pinhole should have the dimension smaller of single spot beam.

An optical photodetector can be modeled easily since it generates a current proportional to the optical power absorbed, in particular

$$I = R(\lambda)P \tag{3.24}$$

where R, which is called responsivity, has a non-linear dependence with wavelength and has a maximum at the design one.

A lot of commercial sensors of this type are available, for example the PDAXXC series from Thorlabs [31]. They are InGaAs switchable gain amplified photodetector and they are available with different responsivities, pinhole sizes and bandwidths (parameter important to detect fast variations of the measured quantity).

The different channels will have random differences in path length that can be modeled assuming the distance of propagation from the fibers to the focusing lens is different for a certain percentage error. When between beams there is constructive interference there will be a maximum in the intensity; instead, when the interference is destructive there will be a minimum. Between two maxima there is a 2π variation in path length. The effect of the phenomenon can be appreciated looking the field along x or y when the channels are spaced (2.4mm in figure Figure 10).

As said in chapter 2.5 the on-axis far field intensity of coherently combined beams should go ideally as N^2, where N is the number of channels. Therefore the intensity ($\propto E^2$) of a single beam with the centroid aligned with the center of the detector has been compared to the one of two overlapped combined beams.

As we can see in Figure 11 from the color scale of the 2D representation of the light intensity on the photodetector this property is verified ($\max(I_2)$ =4×$\max(I_1)$). The width of the combined beams on the target is the same of the one of a single laser giving also a brightness improvement as result.

It must be noted that with the selected lenses, when the distance between the centroids of the beam increases, the efficiency with respect to the ideal case decreases rapidly. Indeed, since the EFL of the focusing lens is 15 mm, the two beams are not enough overlapped on the target and their constructive interference is weaker when they are far from each other.

In Table IV the results with the beams positioned at different distances is reported.

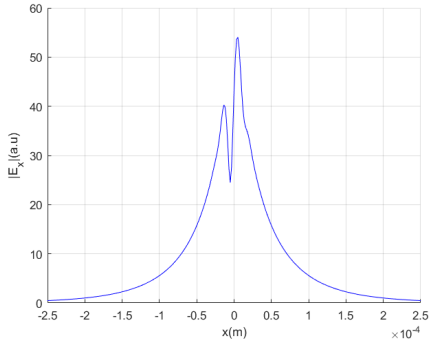

(a) 90° phase variation with respect to the maximum

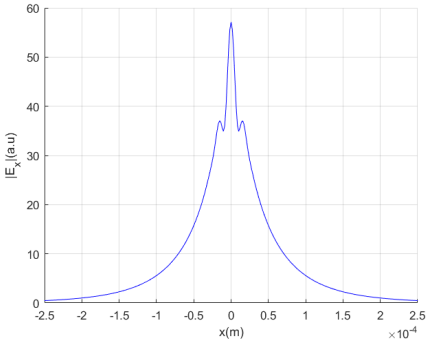

(b) Constructive interference (Max peak)

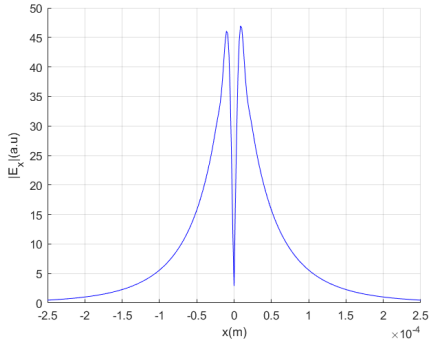

(c) Destructive interference (180° from the maximum)

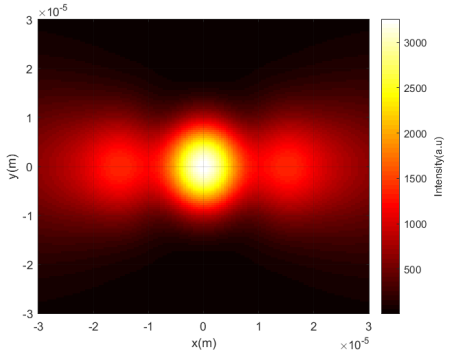

(d) On target 2D intensity when constructive interference is maximized

Figure 10: Effect of path length variation on the combined field

In a in real application the distance between the beams will be forced by the physical dimensions of the connectors therefore such small distances may not be achievable. An efficiency of 50 % would make the method not worthy. A change in the focusing lens, choosing one with a longer EFL should be enough to solve the problem. For example, considering a lens with a

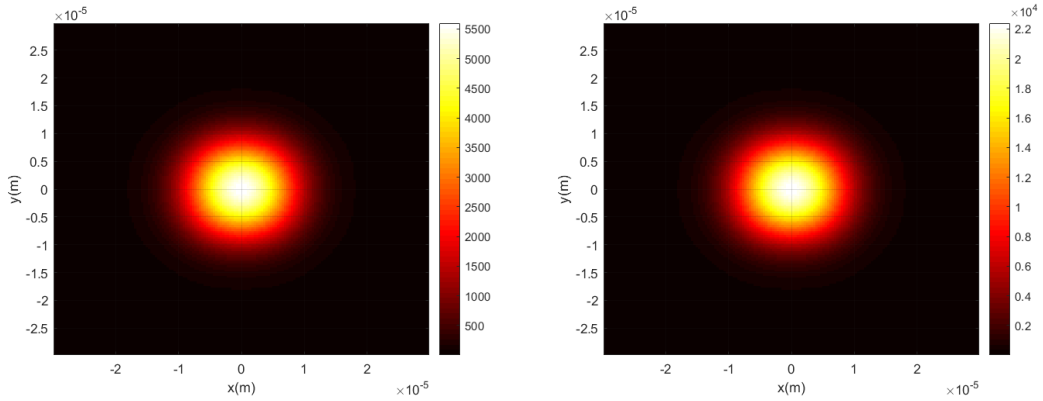

Figure 11: On the left: single beam intensity; on the right: two coherently combined beams intensity

TABLE IV: FOCAL LENGTH 15 mm

Distance(mm)	Distance(w0)	Efficiency
0	0	$N^2 = 4 = 100$ %
0.2	0.21w0	98 %
0.6	0.63w0	88 %
1	1.05w0	71 %
1.4	1.47w0	51 %

focal length of 750 mm the efficiency is way less sensible to distance changes as it can be seen in Table V.

Further changes in the lens can be applied to obtain the desired efficiency if it still not satisfying.

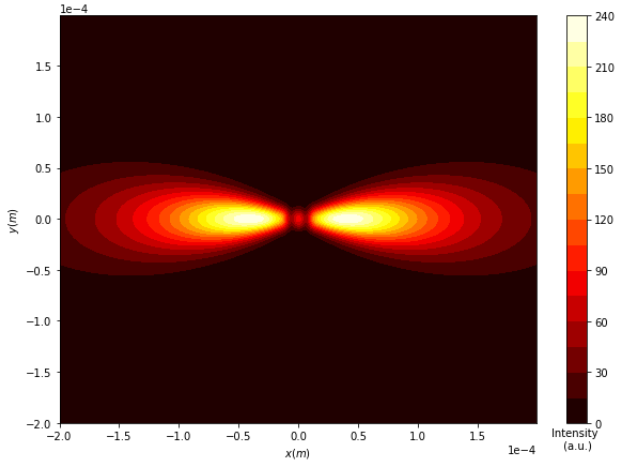

Figure 12: Beams distance 10 mm

TABLE V: FOCAL LENGTH 750 mm

Distance(mm)	Distance(w0)	Efficiency
0	0	$N^2 = 4 = 100$ %
4	4.21w0	98 %
8	8.43w0	77 %
10	10.53w0	66 %

Another problem that appears is linked to the limit of tiled combining: when the distance between beams increases the power in the central lobes of the interference decreases and transfers to sidelobes decreasing the beam quality. The loss is substantial, in particular for single mode fibers that have Gaussian beam profile as shown also in [32] where the central lobe of 4 combined beams contains around 63% of the total power.

As mentioned in Section 2.5, this problem could be solved with a filled aperture which combines the beams in the near field. The filled aperture alignment and set up are more difficult with respect to the tiled case and strong requirements are needed for the combining element. For these reasons this configuration has not been considered in the simulation.

In Figure 13 it is visible the far field pattern on the target when the distance between the beams is 10 mm.

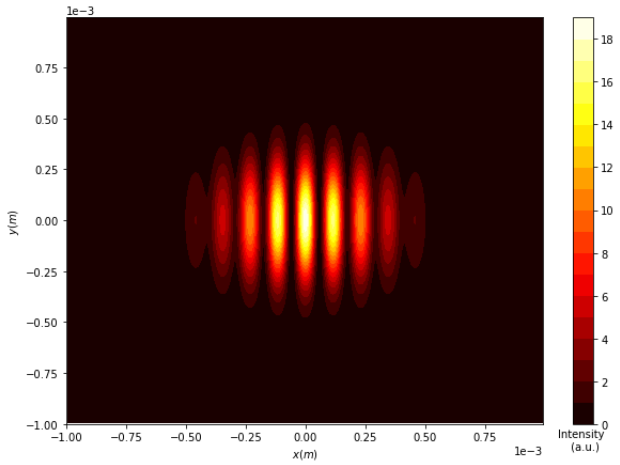

Figure 13: Far field pattern

CHAPTER 4

OPTIMIZATION ALGORITHM

As previously said the path lengths of the beams are subject to random variations which will induce changes in the phase relation. To obtain coherence combination this relation must be optimized and kept stable during operation.

In Chapter 2 different methods of active phase control have been mentioned and it has been decided to try to implement the solution with an hill climbing method.

This choice is due to different reasons:

- in a real set up it can be implemented by means of a DAQ system or an FPGA and it does not require high frequency modulation devices like in the LOCSET technique;
- it is scalable to a greater number of channels;
- differently from the heterodyne method, it requires just one photodetector;
- it can correct multiple types of aberration simultaneously as tip/tilt control, as done for example in [33];
- it involves an algorithm so it can be simulated easily.

Hill climbing methods are a class of optimization algorithms[34]. In a finite set X of possible configurations each configuration is assigned a value called cost; in this way it is possible to define a cost function $J : X \to \mathbb{R}$. For each of configuration, a set of neighbors is defined. The

aim of the algorithm is to find a $xmin/xmax \in X$ to minimize/maximize the cost function depending on the cost difference between neighboring configurations.

The considered system is stochastic, which means: "*is a dynamic system in which the state changes randomly*"[35]. Indeed, when the system is active it will be subject to: random changes in path length, noise due to heating, random fluctuations in polarization and other type of disturbances. All of these changes will contribute to change the final output of the system. The algorithm needs to be able to optimize such a system.

A commonly used hill climbing methods in control algorithm for optical system is the so called Stochastic Parallel Gradient Method (SPGD) [36] and it is able to solve the mentioned problem in such a way efficiency and costs are improved.

4.1 Stochastic Parallel Gradient Descent

The algorithm is a gradient method. They are a class of iterative algorithms that can find local minimum/maximum of differentiable functions. At each iteration a step proportional to the gradient of the cost function during current iteration is taken.

We can consider the cost function to be

$$J(x_1, x_2...x_3) \tag{4.1}$$

where x_i is the ith variable on which the function depends. Then, considering the objective of the algorithm is to maximize the cost function, the gradient method operates as following: each iteration x(i) is updated as [35]

$$x_{i+1} = x_i + \gamma \frac{\partial J(x_i)}{\partial x_i} \qquad i = 1 \ \ldots \ N \tag{4.2}$$

where the coefficient γ is called step size or gain.

It can be seen the method requires the evaluation of the derivatives but, since in the system under analysis is stochastic, the closed form of the cost function will not be known. Then the derivative must be computed numerically. This can be done by exploiting the derivative definition by means of the central difference formula

$$\frac{\partial J(x_i))}{\partial x_i} = \lim_{h \to 0} \frac{J(x+h) - J(x-h)}{2h} \tag{4.3}$$

The functions J(x+h) and J(x-h) will be estimated numerically in the simulation and h will not be 0 but a small number, introducing approximation errors which cannot be avoided.

According to this method for each x(i) a partial derivative need to be computed. Therefore, on each step $2N$ functions would need to be evaluated, requiring a lot of computational time.

The two function evaluations are

$$J(x_1, x_2, \ \ldots x_i + h, x_n) \tag{4.4}$$

$$J(x_1, x_2, \ ...x_i - h, x_n) \tag{4.5}$$

with the ith derivative being

$$\frac{\partial J(x_i}{\partial x_i} = \frac{J(x_1, x_2, \ ...x_i + h, x_n) - J(x_1, x_2, \ ...x_i - h, x_n))}{2h} \tag{4.6}$$

In this type of optimization, the value h is called perturbation since the variable is changed slightly from its value. To avoid the cost of a high number of evaluations the method of parallel or simultaneous perturbations is exploited. At each iteration all the variables x(i) are perturbed of a value h(i) and then just 2 function evaluations are required: the one with all positive perturbations

$$J_+ = J(x_1 + h_1, x_2 + h_2, ...x_i + h_i, x_n + h_n) \tag{4.7}$$

and the symmetric one

$$J_- = J(x_1 - h_1, x_2 - h_2, ...x_i - h_i, x_n - h_n) \tag{4.8}$$

Hence, the formula to compute the derivatives as noted in [37] becomes

$$\frac{\partial J(x_i)}{\partial x_i}\Big|_{x=x_c} = \frac{J_+ - J_-}{2h_c(i)} \tag{4.9}$$

where $x_c(i)$ and $h_c(i)$ are the x(i) and h(i) current values.

Then the variables x(i) are updated as in the classical gradient method following Equation 4.2.

Finally, the stochastic version is different from the classical one because it generates and exploits random variables. In this case the perturbations $h_c(i)$ can be written as

$$h_c(i) = \sigma_c * H_c(i) \tag{4.10}$$

where σ_c is called perturbation coefficient and $H_c(i)$ is a random variable that follows the Bernoulli distribution and can assume opposite values in sign(e.g -0.5, 0.5). The perturbation coefficient (σ) and the step size (γ) must be tuned during the operation to ensure convergence, to increase the speed of the algorithm and the precision of the solutions.

Now that is clear how the method works, a cost or evaluation function must be chosen to be optimized. Different experiments have been done on coherent combination exploiting the SPGD algorithm and different cost functions have been selected.

Commonly used metrics are [38]

$$J1 = \frac{\int\int \sqrt{(x-x0)^2 + (y-y0)^2} I(x,\ y)\ d_x d_y}{\int\int I(x,\ y)\ d_x d_y} \tag{4.11}$$

$$J2 = \int\int I^2(x,\ y) \tag{4.12}$$

$$J3 = \int\int_{\mathcal{R}} I(x,\ y) \tag{4.13}$$

$$J4 = \frac{I_{max}(x,\ y)}{I_{maxtheory}(x,\ y)} \tag{4.14}$$

In these formulas:

- I(x,y) is the light intensity on the target which is proportional to $|E(x,y)|^2$;
- x_0 and y_0 are the light intensity distribution centroids;
- Equation 4.11 is probably the most effective metric [39] since it gives both information about position and light intensity.
- Equation 4.14 is also known as Strehl ratio and compares real performance with respect to ideal ones: therefore, it is usually a beam quality evaluation parameter.

To keep the model simpler, the metric in Equation 4.13, which is also called encircled energy. has been chosen as cost function for our simulation with $\mathcal{R}$ being the region where maximum energy is collected (the photodetector area)

The SPGD algorithm needs to be adapted to the experiment. Indeed, it is necessary to understand how it can be implemented in the control loop. In Figure 4 it can be seen that only the photodetector is connected directly to the control electronics. This means that the controller will receive just an analog current. An ADC is then required to convert it to digital domain, in which the algorithm can be applied. Considering the evaluation function J, it is known that it will be a function of the phase of the single beams. Since the EOMs have been introduced in the system, J3 will be actually a function of the applied voltages to each EOM J(u(1),u(2),...,u(n)).

The voltages are applied through an ad hoc driver usually supplied by the producer of the EOMs. The controller must be able to send the signals to generate the correct voltages.

The algorithm starts with initial applied voltages $u^1 = \{u(1), u(2), ..., u(n)\}$. In order to find the optimal starting point the convergence of different runs should be observed. At first, all the starting voltages are set to be null.

For each iteration of the algorithm the following steps need to be followed:

1. Generate Bernoulli-distributed random independent perturbations which are then transformed into random voltages $\delta u^i = \{\delta u^i(1), \delta u^i(2)...\delta u^i(n)\}$ from the driver (where i is the iteration number, while n is the number of channels(
2. Apply the positive perturbations to the modulators and measures $J_+ = J(u + \delta u)$.
3. Apply the negative perturbations and measures $J_- = J(u - \delta u)$.
4. Compute the difference $\Delta J = J_+ - J_-$ needed to obtain the derivatives.
5. Update the voltages as

$$u(k)^{i+1} = u(k)^i + \frac{\gamma}{\sigma^2}\frac{\Delta J}{J_{max}} * \delta u(k)^i \tag{4.15}$$

where J_{max} is the maximum of the cost function obtained in open loop; the gain γ should be a value between 0 and 1; the Bernoulli perturbations should be function of σ or, in other words, the values which the δu can assume are $-\sigma$ or $+\sigma$. Both the perturbation amplitude and the gain can be updated during the operations to change the speed of

convergence and increase the precision when the cost function is closed to the maximum and to avoid oscillations around it.

As it can be seen the computation of the gradient in Equation 4.15 and reported in [40] is a bit different with respect to the definition given in Equation 4.2. In literature a bit of discrepancies is found around this function: in [33] it is used

$$u(k)^{i+1} = u(k)^i + \gamma \frac{\Delta J}{2} \delta(k)^i \tag{4.16}$$

while in [41] instead

$$u(k)^{i+1} = u(k)^i + \gamma \Delta J \delta u(k)^i \tag{4.17}$$

All of these are valid solutions, but in the specific case of the implemented simulation the one in Equation 4.15 has been found to be more effective and the following results are reported with respect to it.

4.2 Validation of the algorithm

To validate the algorithm different scenarios have been tested. At the beginning the two channels are positioned in the overlap condition (no distance between the centroids of the beams) of Figure 11 and they have been set to have a starting random phase relation. For now, no random variations have been considered during operations.

The optimization has been run with different perturbation amplitudes σ and gain γ (ranging between 0 and 1). It has been observed that when the gain is higher the algorithm converges faster. After several testing, $\sigma = 0.5$ has been taking as starting perturbation amplitude. When

the cost function J gets to a certain percentage of J_{max}, σ is reduced while keeping $\frac{\gamma}{\sigma^2 * J_{max}}$ constant. This means that the gain is changed accordingly. In certain cases, it oscillates around the maximum because the step to update the voltages is too big. In these cases it is required to reduce the starting gain and restart the algorithm. Once the tuning of gain and perturbation amplitude is done for the configuration the algorithm in this condition always converges.

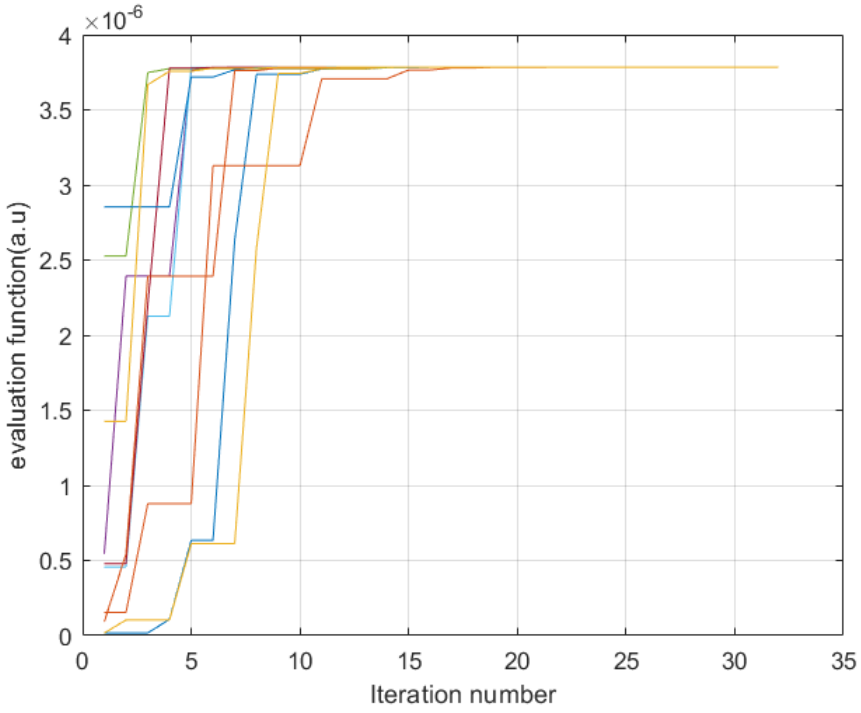

Figure 14: Convergence with 10 different starting phase errors, beams in the overlap condition

In Figure 14 it can be seen that no matter which is the phase difference, the algorithm converges in a few iterations. Indeed, it is able to correct the relation even in the worst condition when $\Delta\phi = \pi$. One of the limits of gradient methods is that they are not guaranteed to converge to the global maximum. Indeed the algorithm can get "trapped" in a local optima and for its structure it is not able to get out from this condition. For this reason the maximum value of the optimized evaluation function has been double checked with the open loop simulation. It has been seen that the value is correct indicating the algorithm is not falling in another local maximum. This was expected because there is only a phase condition were the beams are perfectly coherently combined and therefore the only maximum should be the global one.

Another parameter that need to be considered is the convergence time. On each iteration of the algorithm the voltages applied to the EOM are changed three times. Once to apply the positive perturbations, once for the negative ones and once to update the voltages for the next iteration. This means that if we select , for example, an updating frequency of the voltages of 6 kHz and we consider the delays introduced by the input ADC, the FPGA, the output DAC, and the RF driver in the order of nanosecond, they will be negligible with respect to the time needed for an iteration.

The time required from a full iteration will be roughly $T_i = 3\frac{1}{6\times10^3\text{Hz}} = 0.5$ ms. Therefore the convergence time in the slowest of the simulated cases shown in Figure 14 would be

$$T_c = 0.5 \text{ ms} \times 15 = 7.5 \text{ ms} \tag{4.18}$$

We can compare this value with the one of similar other set-ups which use this method. For example in Figure 3 of [42] it can be seen that for their experiment the typical convergence time is around 4 ms which is line with the one obtain in our simulation. If faster convergence times are needed, the update frequency can be increased. Since, once the convergence is reached the algorithm is stable and does not move from the maximum, a few millisecond at the beginning of the operations should be an acceptable delay.

To proceed with the validation, the algorithm has been run with a distance between the two beams (as the one reported in Figure 10). Once again also for this case, different random starting phase errors have been simulated.

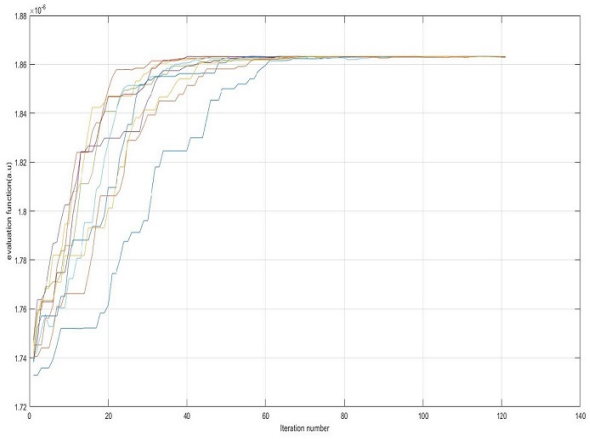

Figure 15: Convergence with 10 different starting phase errors, beams not overlapped

In Figure 15 it can be seen that also in this case the algorithm still converges and is stable afterwards. It has to be noted that the number of iterations needed to find the optimum value of J is higher than the previous one. This is probably due to the fact that, as also mentioned in Section 3.6, when the distance between the beams is increased the efficiency of the combining is less effective. Therefore the variation in the cost function is not as evident as before which leads to a slowdown in the gradient operations. The algorithm has been tested also on more than 2 channels, namely 4 channels, and it presented similar behavior beside an increased number of iterations required. This was expected since ideally the convergence time is $tc \propto \frac{2N}{f_{update}}$.

Once the algorithm has been validated, it has been tested it in a more realistic environment introducing noise in the system. In particular, on each measurement of the cost function J from the photodetector a random noise was generated and added to the phase term to simulate variations that in a real application would be present. This means also that the evaluations of J_+ and $J-$ are affected by noise.

When the introduced noise is a low noise (with Gaussian distribution) the operations are unperturbed and the algorithm converges as in the ideal case. When the noise is increased and is of the same order of magnitude of the perturbation amplitude σ, the convergence is slower but then the cost function is stable as shown in Figure 16. Obviously a very high noise can lead to no convergence. It has been seen, though, that increasing the perturbation amplitude and changing the gain can reduce the algorithm's noise sensibility.

Another problem that the algorithm should be able to solve is to recover the phase relation when an external factor induces a big variation in the cost function while it is stable at its

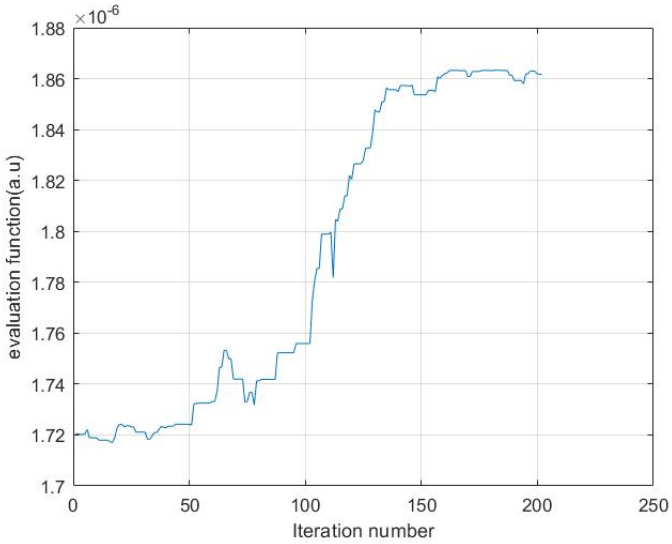

Figure 16: Convergence with high noise

maximum. To simulate such a situation a phase noise following a Laurentz distribution has been exploited. The tails of this distribution are more evident than the ones of the Gaussian. In this way the probability of a big phase variation is increased.

As we can see in Figure 17 the cost function after reaching the optimal value presents big oscillations induced from the noise. The algorithm in few iterations recover the correct phase relation. The system should be then insensitive to external factor induced variations if they are single events and they are not reiterated in a short amount of time.

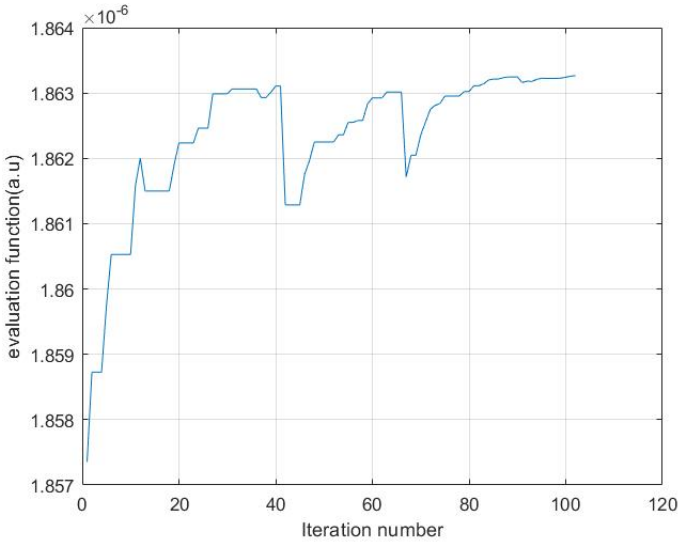

Figure 17: Convergence with Laurentz distributed noise

CHAPTER 5

EXPERIMENT ON SPECTRAL BEAM COMBINING

In this chapter an experiment on spectral combining is described. Spectral or wavelength combining as mentioned in chapter 2 is a technique that aims to increase the power emitted from multiple lasers while maintaining the beam quality of a single one and, thus. increasing also the brightness.

With respect to coherent combining it does not require mutual coherence between the combined beams and it is usually less sophisticated to be implemented. The main difference in the combined beams of the two techniques is that a spectral combined output has usually a larger spectrum. If a narrow line output it is not required such as in very precise pumping applications spectral combining should be preferred to the coherent one.

The lasers under investigation in the experiment are high power diodes with emission wavelength in the blue range of the visible spectrum (440-495 nm). Blue semiconductor lasers are an under development technology in high power industry. They are being studied since they have different properties (such as high electrical to optical conversion efficiency and lower cost) that could make it a contender of the nowadays most used infrared lasers in material processing applications. The blue diodes substrate material is GaN and due to its properties they usually reach lower maximum power than the infrared ones. A blue high power diode can emit up to 4 W [43] while, as mentioned in section 2.2, tapered lasers in the infrared can reach 12 W. For

this reason it is important to investigate ways of scaling their power such as wavelength beam combining.

5.1 Description of the Experiment

The idea for the experiment is proposed in a patent from Teradiode inc.[44] where three variations of wavelength beam combining are presented. In particular in fig 1A shows a set-up to combine the beams coming from a diode bar. A diode bar is linear 1D array of semiconductor lasers placed near to each other.

The system described is the following:

- A diode bar composed of multiple elements each emitting at a slightly different wavelength from the others. Each emission bandwidth of the single diodes must be a small fraction of the gain bandwidth to efficiently be combined. To achieve a good beam quality the lasers should be as close as possible. The minimum distance between the diodes is forced from the need of cooling the bar; usually heat sinks are inserted for this purpose.
- A single collimating optic is used to collimate the beam along the fast axis.
- A cylindrical or spherical lens is used to combine the beams and focus them onto a dispersive element.
- The dispersive element is a diffraction grating which transmits the beams to a partially reflective output coupler. It is placed at the BFL of the focusing lens otherwise an output beam quality degradation will appear.

- The partially reflecting coupler is positioned onto the path of the first order of the diffraction grating in such a way it can provide feedback for the wavelength control of the diodes.
- Ideally the output power should be the sum of the powers of the single diodes preserving the beam quality of a single one.

The actual implementation in the laboratory, which has some variations with respect to the previously describes set up, is shown in Figure 18. In this experiment the objective was to demonstrate the possibility of self-locking of multiple diodes by means of feedback from the first order of the diffraction grating.

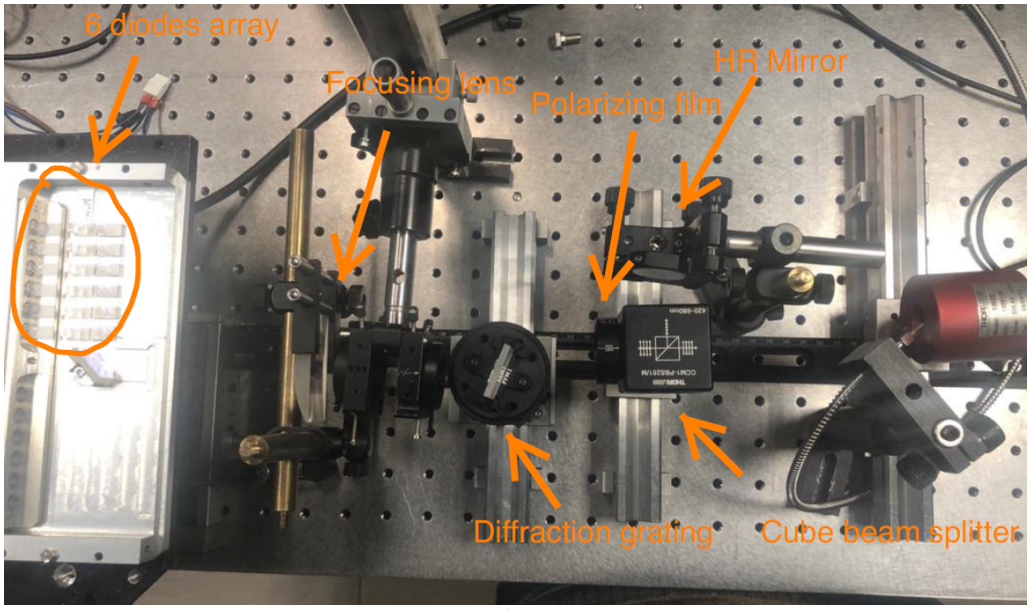

Figure 18: Laboratory set-up

The emitting module is composed from a diode bar made of 6 equally spaced blue diodes. On the module each beam is collimated in two stages: at first the fast axis (faster divergence) and after the slow axis. The collimated beams, by means of angled incidence on multiple mirrors are transmitted to a coupler. The output from the coupler is then sent to the transforming optic which is a cylindrical lens from Edmund Optics. The lens (stock number #69738) is a 50 mm $\times$ 25 mm lens with an EFL of 150 mm, BFL of 146.51 mm with an antireflecrtive coating from 425 nm to 675 nm.

The beams are focused on a GT25-03 blazed transmission gratings from Thorlabs placed at the BFL of the lens. A blazed grating is designed to transmit maximum power on a specific order while minimizing the loss on the other ones. In particular, the selected one has the highest transmission efficiency on the 1st order.

It was possible to choose grating with different grooves spacing. The maximum efficiency at 450 nm is around 55 % and can be obtained with the 300 mm grooves as it can be seen from the graph provided by the supplier[45]. To achieve this efficiency the grating must be positioned with the correct inclination with respect to the optical axis.

This positioning of the grating is called Littrow configuration. The light is incident on the grating at a specific angle(θ_L) which can be derived from

$$2a\sin(\theta_l) = m\lambda_0 \tag{5.1}$$

where a is the spacing between the grooves, m the highest efficiency order and λ_0 is the design wavelength.

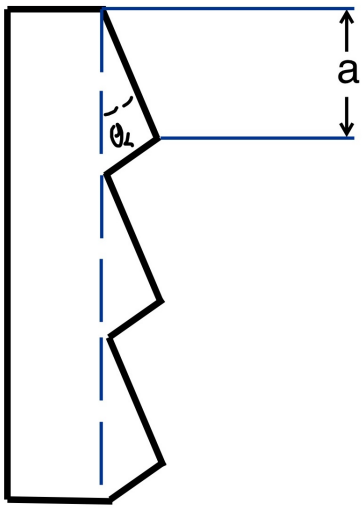

Figure 19: Blazed grating

It can be shown that the Littrow angle is equal to the blaze angle given from specifications and is $\theta_l = 17.5^o$. In Figure 18 it can be seen the grating is tilted of this angle with respect to the perpendicular of the optical axis.

When the first order of the transmission grating is fed back into the diodes, the emission wavelength will be changed due to a "combination of the standing wave condition, cavity length and the center wavelength of the grating feedback,i.e., a grating angle"[46]. This is because

a mode hop of the longitudinal modes of the laser occurs. The mod hops can happen when between the reflected laser frequency imposed from the grating

$$\nu_g = \frac{c}{2a\sin(\theta)} \tag{5.2}$$

and the modal frequency ν_m holds the following relation:

$$|\nu_m - \nu_g| \geq \frac{1}{2}\frac{c}{2L} = \frac{FSR}{2} \tag{5.3}$$

where FSR is the free spectral range.

The reflected frequency can be changed adjusting the feedback mirror (which has 3 degrees of movement) and therefore the incidence angle on which it depends. This variation in ν_m can cause mode hops. This technique of forcing mode hopping is also called wavelength locking. Ideally each diode should lock himself at a slightly different wavelength from the others narrowing the overall spectrum and forming a single combined beam on the output coupler with increased brightness.

On the path of the 1st order of the grating it has been placed a 50/50 polarization beam splitter. Before the cube it has been inserted a rotatable polarizing film. The emissions from the diodes of the module are almost totally TE mode, when the combined beam is incident on the film the polarization becomes partially TM and partially TE. When the film is rotated the percentage of the beam to be TE and TM can be changed. The polarization beam splitter transmits on one output the TM mode and the TE mode on the other one.

The TM output is reflected on a high reflectivity mirror and it is sent back as feedback to the diodes. Going back through the splitter and the polarizing film the polarization turns again in TE mode. The TE output, instead, is incident on a power meter (S302C from Thorlabs) and a spectrometer (Avaspec 3648 from Advantest). The power meter is needed to tune the feedback power when rotating the polarizing film while the spectrometer allows to observe the spectrum of the output beam.

5.2 Results

At first the grating efficiency has been characterized in a low power regime (each diodes emit $\sim$ 60 mW). The diode bar is provided with switches to turn-on the diodes individually; therefore the characterization has been done by measuring: at first the total power of the beams of an increasing number of diodes injected with the same current , then the power of the different orders of the grating in the same conditions.

TABLE VI: GRATING ORDERS EFFICIENCIES

Number of diodes	Zero Order Efficiency	First Order Efficiency	Second Order Efficiency
5	13 %	55 %	20 %
6	14 %	52 %	19 %

In Table VI the grating orders' efficiencies are reported for five and six diodes. Since, when only two diodes are turned on, the first order efficiency is equal to 61%, the grating behaves like expected from specification. It has also to be noted that with increasing power the efficiency is decreasing, probably, due to the heating of the grating (no data where provided about power vs efficiency relation from the supplier).

Since the possibility of controlling the emission wavelength with the feedback from the mirror depends from the power that comes back into the diodes , this efficiency deterioration needs to be kept into account. The grating should be changed if such a system is desired to be exploited in a high power application.

The maximum achievable feedback has been measured with two diodes turned on with the polarizing film rotated in such a way that almost the entire output power is sent to the mirror. In the path are important also the passive element losses , taking into account ,beside the mirrors,the light passes through the elements two times before reaching again the diodes.

TABLE VII: PASSIVE LOSSES AND FEEDBACK

Polarizing Film Efficiency	Cube Efficiency	Mirror Efficiency	Total Feedback
85 %	96 %	98 %	23 %

In Table VII are reported the efficiencies of the various passive element. The polarizing film introduces a substantial loss while the effect of the mirror and the polarizing beam splitter are almost negligible. The maximum feedback achievable when almost all the power is reflected is around 23%. This could be a very low value since in a real application a major quantity of the power should be used as output and not as feedback (thus reducing the percentage even more) but for a proof of concept it can be accepted.

The emission (looking Figure 18 the diodes are numbered from the bottom to the top) wavelengths of each lasers has been measured. After that, turning on one diode at a time, they have been self locked singularly with the feedback from the grating. The self and locked wavelength of the diodes are reported in Table VIII. An increase of the wavelength is verified and the diodes lock themselves at slightly different wavelength. The linewidth of the diodes is very narrow and the spectrometer samples just a few points in their bandwidth therefore the value of the locked wavelength is the same for some of them due to low resolution.

TABLE VIII: CENTRAL WAVELENGTH VS LOCKED WAVELENGTH

Diode #number	Central wavelength	Locked Wavelength
1	447.4 nm	449.1 nm
2	446.7 nm	448.8 nm
3	447.1 nm	448.1 nm
4	446,4 nm	448.1 nm
5	446.7 nm	448.8 nm
6	447.1 nm	449.1 nm

Figure 20 shows a comparison between the spectrum of diode 4 in the normal condition and when is locked.

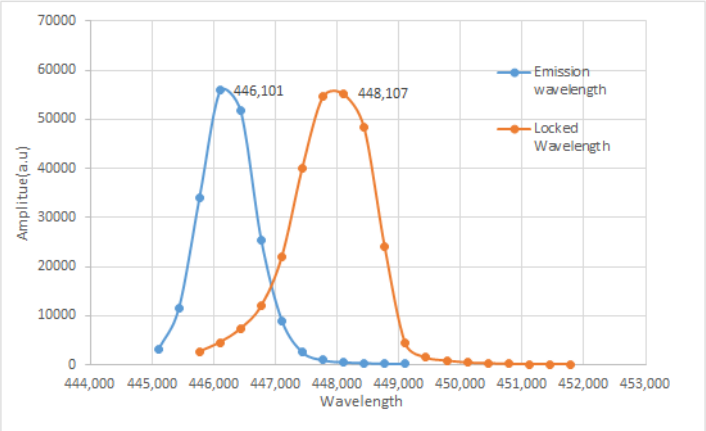

Figure 20: Diode #4 central wavelength vs locked wavelength

Ideally it should be possible to lock all the lasers at the same time. Although the set-up presents some problems:

- there are a lot of mechanical components which introduce uncertainties in the system.
- the alignment of the system which plays an important role in optical experiments is complicated from the fact the selected grating has the maximum power on the first order. The following passive elements need then to be positioned on a different axis with respect

to the one of the focused beam. This implies that is difficult to find the position of the mirror which guarantees the feedback is reaching all the diodes at the same time.

- The mirror should be controlled with very high precision and not be adjusted by hand.
- The path length should be reduced as much as possible to decrease the divergence of the feeedback.
- A focusing lens with a greater BFL could be used to overlap the beams on the grating in a better way.
- The grating should have a greater efficiency to increase the feedback.
- A spectrometer with an increased resolution would make the identification of the locking easier.

Having said that it was possible to lock at the same time 2 lasers , in particular diodes #2 and #3. In Figure 21 the behavior of the diodes while locking can be observed. In the orange plot we can see that one of the diodes is still emitting around its own wavelength while the other is mode hopping between two longitudinal modes. When the correct position of the mirror is found both lock themselves around 448.1 nm. The wider shape actually indicates that the locked wavelengths of the two beams is slightly different, as it was expected.

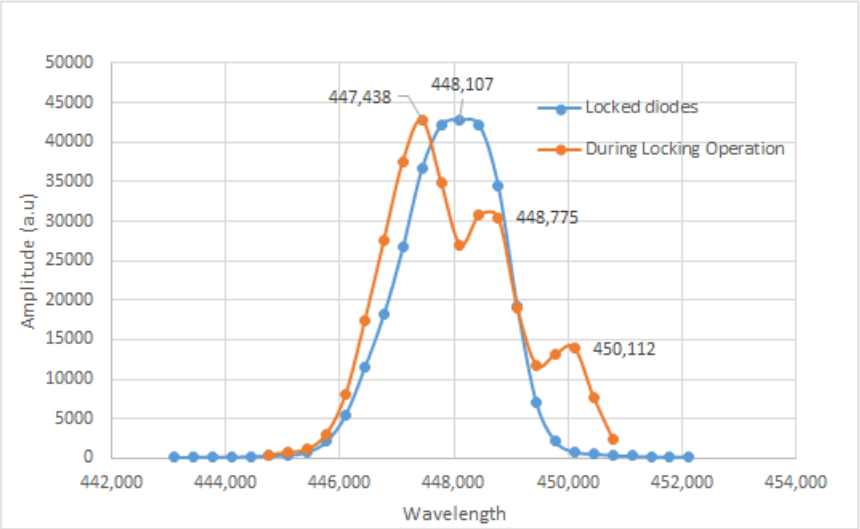

Figure 21: Diode #2 and #3 during and after locking

The objective of the experiment has then been reached: with the proposed set up it is possible to self lock the diodes wavelength by means of the feedback from the first order of diffraction grating for a spectral combining application. An improvement of the set up could permit to lock more diodes together

CHAPTER 6

CONCLUSION

In this thesis the state of the art reached by laser diodes technology has been discussed and it has been explained the reason why techniques for power scaling and brightness enhancement are needed. Different beam combining techniques such has spatial, spectral beam and coherent combining have been reviewed and previous research works have been presented.

Coherent beam combining techniques and the pros and the cons of the different approaches have been analyzed. Passive coherent combining is of easy implementation since it consists just in a cavity design and has self adjusting phases due to resonance behavior. This method can improve the brightness but has low scalability regarding the number of combined diodes and even if good efficiency has been achieved it is not suitable for high power applications.

Active coherent combining is more complex and requires non linear devices such as electro-optic or acousto-optic modulators and real time active correction of the phase. The most common configuration is the MOPA one where N channels are seeded from the same laser amplified and then combined while maintaining the same phase relation trough active feedback. For MOPA three methods are usually exploited for phase locking: heterodyne , SPGD correction, LOCSET. Each of these three has advantage and disadvantage which have been reported in table Table I. For its lower cost, good scalability, flexibility on the type of correction and easy implementation the SPGD method has been chosen for a possible implementation.

As original work a full numerical simulation of a MOPA system and a spectral beam combining experiment have been performed.

Regarding the MOPA system, at first the system has been analyzed in open loop with the phase relation tuned without the algorithm. It has been supposed to have N fibers seeded by the same laser and with an ideal Gaussian output. The beams have been collimated and focus onto a target and the deterioration of the combining efficiency due to lenses and the positioning of the beams has been discussed. When the beams are mutually coherent and overlapped the light intensity is N^2 times the one of a single beam as expected from theory. When the phase relation is not correct they can interfere destructively obtaining a reduction of the intensity peak which is not to be desired. When the beam are spaced the efficiency decrease due to the reduction of the coherence relation. With the right choice of the focusing lens to increase the spatial overlap of the beams in the far field the efficiency sensibility to this variation can be reduced. In the whole simulation the used dimension of fibers, collimators, focusing lenses and the photodetector have been set following the ones of available commercial devices.

Introducing a random phase variation between the channels, the SPGD algorithm to actively correct the phase has been written and validated on Matlab. The cost function chosen for the optimization was the encircled energy. In ideal scenarios, after the tuning of the parameters (γ and σ) the algorithm always converges in few iterations and in times comparable with other similar experiments.

The algorithm has been tested also under different noise disturbances. Low noise sources have no effect on the convergence, higher sources can increase instead the convergence time.

The algorithm can also correct isolated critical phase changes due to external factor. It has also been observed the parameters can also be tuned to reduce noise sensibility.

As for the spectral beam combining experiment, the set-up consists of a module of 6 diodes collimated and focused onto a blazed diffraction grating. The first order of the grating is then used as feedback to lock the wavelength of multiple diodes. The locking of each diodes on a different wavelength from its own emitting one has been demonstrated as well as the contemporary locking of two diodes. This shows the validity of the method which can be improved solving some of the problems which the set-up presents. Among all, the grating should be changed with one of a greater efficiency and the degrees of freedom of the system should be decreased to reduce the mechanical and alignment errors.

Future works should be aimed to: improve the simulation of the coherent combining experiment with finer details and to test it in laboratory in a real application; improve the spectral beam combining experiment trying to lock more diodes together and measure the brightness of the output.

Laser power scaling has been and still is a trending research topic of the last years and we hope this study can be confirmed or questioned by other research works and conclusions.

APPENDICES

Appendix A

OPEN LOOP ANALYSIS CODE

Below is listed part of the code used for the open loop analysis:

```
clc
close all
clear all
%Gaussian Beam
%E(x,y,z)=E0{w0/w(z)(exp(-r^2/w^2(z))exp(-j(kz-arctg(z/z0)))exp(-jkr
    ^2/2R(z))
%Phase factor exp(-j(kz-arctg(z/z0)))
%Radial phase factor exp(-jkr^2/2R(z))
%With
%w^2(z)=w0^2(1+(z/z0)^2
%R(z)=z(1+(z0/z)^2)
%z0=kw0^2/lambda0
E0_1=1;
E0_2=1;
%Wavelength
lambda=1550e-9;
```

Appendix A (continued)

```
16 %focusing lens radius
17 xlens=5e-3;
18 %Fourier parameters
19 NFFT=2^12;
20 N=NFFT/2;
21 Wx=1e-2;
22 yvet=[-N:N-1]*Wx/NFFT;
23 xvet=([-N:N-1]*Wx/NFFT)';
24 fxvet=([-N:N-1]/Wx)';
25 fyvet=[-N:N-1]/Wx;
26 %centroid coordinates
27 mu_x=0.5e-3;
28 mu_x2=-0.5e-3;
29 mu_y=0.5e-3;
30 mu_y2=-0.5e-3;
31 %Collimating Lens Focal Length
32 fc=10*1e-3
33 %Focusin Lens Distance
34 d=1e-2
35 %Refractive Index of Propagating Medium
36 n=1;
```

Appendix A (continued)

```
37 %Wave Number
38 k=2*pi*n/lambda;
39 %Cladding diameter 125 um Coating 245 um
40 MFD=10.4e-6 %Mode field diameter fibra PM 1550
41 % Beam Waist After Collimator
42 w0=2*lambda*(fc/(pi*MFD));
43 %Raleigh Distance
44 z0=pi*w0^2/lambda
45 %Plano Convex Focusing Lens
46 %Radius of Curvature
47 R1=7.7e-3;
48 %Refractive Index
49 nl=1.515;
50 %Focal Length
51 ff=15e-3
52 %Thickness of Convex Part
53 Delta01=0.6e-3;
54 %Central Thickness
55 Delta02=1.5e-3;
56 T_tot=Delta01+Delta02;
57 %Distance of Propagation Channel 1
```

Appendix A (continued)

```
58 z=d;
59 %Percentual Phath Length Error Between The Channels
60 perc=0;
61 Deltaz=d*perc/100;
62 %Distance of Propagation Channel 2
63 z2=z+Deltaz;
64 %Beam Waist at the Focusing Lens
65 w=sqrt((w0^2)*(1+(z/z0).^2));
66 w2=sqrt((w0^2)*(1+(z2/z0).^2));
67 %Radius of Curvature of the Pase Front
68 R= z.*(1+(z0./z).^2);
69 R2=z2.*(1+(z0./z2).^2);
70 %Propagation of the Field and Application of the Focusing Lens Phase
71 %Function
72 E=((E0_1.*(w0./w).*exp(-(sqrt((xvet-mu_x).^2+(yvet-mu_y).^2)').^2./w
       .^2)).*exp(-1j.*(k.*z-atan(z/z0))).*exp(-1j*k.*(sqrt((xvet-mu_x)
       .^2+(yvet-mu_y).^2)').^2./(2*R))...
73      +(E0_2.*(w0./w2).*exp(-(sqrt((xvet-mu_x2).^2+(yvet-mu_y2).^2)')
           .^2./w2.^2)).*exp(-1j.*(k.*z2-atan(z2/z0))).*exp(-1j*k.*(sqrt
           ((xvet-mu_x2).^2+((yvet-mu_y2)).^2)').^2./(2*R2)))...
```

Appendix A (continued)

```
74        .*exp(1j.*(k*((nl-1).*(Delta01-(R1-sqrt(R1^2-xvet.^2-yvet.^2))+
              Delta02)+T_tot)'));
75  %Set Field Outside the Lens to 0
76  i= find(abs(xvet)>xlens);
77  E(i,i)=0;
78  figure(6)
79  plot(xvet,abs(E(2049,:)))
80  % Angular Spectrum Propagation
81  E=fftshift(fft2(fftshift((fftshift(ifft2(fftshift(E)))*Wx*Wx).*exp
        ((1j*2*pi/lambda).*(sqrt((1-(lambda.*fxvet).^2)-(lambda.*fyvet)
        .^2)*ff)))))/(Wx*Wx);
82  %Photodetector
83  %Pinhole  Radius
84  xpd=100e-6
85  pd_index=find((abs(xvet)<xpd));
86  %Intensity
87  I=(abs(E(pd_index,pd_index))).^2;
88  a=trapz(yvet(pd_index),I);
89  %Power Collected on the Detector
90  P=trapz(xvet(pd_index),P);
91  R_1550=1 ;% 1 A/W
```

Appendix A (continued)

```
92 %PhotoDetector Output Current
93 Ipd=P*R_1550;
94 J=Ipd;
```

Appendix B

SPGD IMPLEMENTATION

```
%Half Drive Voltage of the EOM (V)
Vpi=3.24;
%SPGD Alghoritm
%Max of the Evaluation Function Measured in Open Loop
J_max=Ipd
metric(1)=J_start;
%gain
gamma=0.9
%perturbation amplitude
sigma=0.5
xi=gamma/(sigma^2*J_max)
c=sigma
%Perturbation Voltage
deltau=sigma*binornd(1,0.5,1,2); %bernoulli with 0 mean
 i=find(deltau==0);
 deltau(i)=-sigma;
u_old=0;
```

Appendix B (continued)

```
18 u_new=0;
19 o=1;
20 flag=0;
21 J_old=0.5*J_start;
22 %noise deviation
23 noiseamp=0;
24 while(flag==0)
25 %Laurentzian noise
26 %noisephi=cauchyrnd(0,noiseamp,1,2)
27 %Gaussian noise
28 %noisephi=normrnd(0,noiseamp,1,2);
29 %No Noise
30 noisephi=zeros(2);
31 %Application of the Positive Perturbation to the EOM
32 varphi=EOM(u_new+deltau,Vpi);
33 %J+ measurement
34 E=(E0_1.*(w0./w).*exp(-(sqrt((xvet-mu_x).^2+(yvet-mu_y).^2)').^2./w
       .^2)).*exp(-1j.*(k.*z-atan(z/z0))).*exp(-1j*k.*(sqrt((xvet-mu_x)
       .^2+(yvet-mu_y).^2)').^2./(2*R))*exp(1j*varphi(1))*exp(1j*
       noisephi(1))...
```

Appendix B (continued)

```
35        .*exp(1j.*(k*((nl-1).*(Delta01-(R1-sqrt(R1^2-xvet.^2-yvet.^2))+
              Delta02)+T_tot)'))...
36  +((E0_2.*(w0./w2).*exp(-(sqrt((xvet-mu_x2).^2+(yvet-mu_y2).^2)')
        .^2./w2.^2)).*exp(-1j.*(k.*z2-atan(z2/z0))).*exp(-1j*k.*(sqrt((
        xvet-mu_x2).^2+(yvet-mu_y).^2)').^2./(2*R2)))*exp(1j*varphi(2))*
        exp(1j*noisephi(2))...
37        .*exp(1j.*(k*((nl-1).*(Delta01-(R1-sqrt(R1^2-xvet.^2-yvet.^2))+
              Delta02)+T_tot)')));
38  i= find(abs(xvet)>xlens);
39  E(i,i)=0;
40  E=fftshift(fft2(fftshift((fftshift(ifft2(fftshift(E)))*Wx*Wx).*exp
        ((1j*2*pi/lambda).*(sqrt((1-(lambda.*fxvet').^2)-(lambda.*fyvet)
        .^2)*ff)))))/(Wx*Wx);
41  I_pert=(abs(E(pd_index,pd_index))).^2;
42  Px_pert=trapz(xvet(pd_index),I_pert);
43  P_pert=(trapz(yvet(pd_index),Px_pert));
44  R_1550_pert=1 ;% 1 A/W
45  Ipd_pert=P_pert*R_1550_pert;
46  %Energy detected  J proportional to Ipd^2
47  J_plus=Ipd_pert;
48  %%%%%%%%%%%%%%%%%%%%%%%%%%%%%%%%
```

Appendix B (continued)

```
%Laurentzian noise
%noisephi=cauchyrnd(0,noiseamp,1,2)
%Gaussian noise
%noisephi=normrnd(0,noiseamp,1,2);
%No Noise
 noisephi=zeros(2);
%Application of the Negative Perturbation to the EOM
 varphi=EOM(u_new-deltau,Vpi);
%J- measurement
E=(E0_1.*(w0./w).*exp(-(sqrt((xvet-mu_x).^2+(yvet-mu_y).^2)').^2./w
    .^2)).*exp(-1j.*(k.*z-atan(z/z0))).*exp(-1j*k.*(sqrt((xvet-mu_x)
    .^2+(yvet-mu_y).^2)').^2./(2*R))*exp(1j*varphi(1))*exp(1j*
    noisephi(1))...
     .*exp(1j.*(k*((nl-1).*(Delta01-(R1-sqrt(R1^2-xvet.^2-yvet.^2))+
        Delta02)+T_tot)')))...
+((E0_2.*(w0./w2).*exp(-(sqrt((xvet-mu_x2).^2+(yvet-mu_y2).^2)')
    .^2./w2.^2)).*exp(-1j.*(k.*z2-atan(z2/z0))).*exp(-1j*k.*(sqrt((
    xvet-mu_x2).^2+(yvet-mu_y).^2)').^2./(2*R2)))*exp(1j*varphi(2))*
    exp(1j*noisephi(2))...
     .*exp(1j.*(k*((nl-1).*(Delta01-(R1-sqrt(R1^2-xvet.^2-yvet.^2))+
        Delta02)+T_tot)')));
```

Appendix B (continued)

```
62 i= find(abs(xvet)>xlens);
63 E(i,i)=0;
64 E=fftshift(fft2(fftshift((fftshift(ifft2(fftshift(E)))*Wx*Wx).*exp
       ((1j*2*pi/lambda).*(sqrt((1-(lambda.*fxvet').^2)-(lambda.*fyvet)
       .^2)*ff)))))/(Wx*Wx);
65 I_pert=(abs(E(pd_index,pd_index))).^2;
66 Px_pert=trapz(xvet(pd_index),I_pert);
67 P_pert=(trapz(yvet(pd_index),Px_pert));
68 R_1550_pert=1 ;% 1 A/W
69 Ipd_pert=P_pert*R_1550_pert;
70 J_minus=Ipd_pert;
71 %Difference between J+ and J*
72 deltaJ=J_plus-J_minus;
73 %Control Voltage Updates
74 u_new=u_old+xi*deltaJ*deltau;
75 u_old=u_new;
76 %Parameters Tuning to Increase Resolution when Reaching the Optimal
       Value
77 if J_old<0.7*J_max
78       sigma=0.5;
79
```

Appendix B (continued)

```
80   elseif   J_old >=0.9*J_max && J_old<J_max
81         sigma=0.2;
82   end
83  gamma=xi*sigma^2*J_max;
84   deltau=sigma*binornd(1,0.5,1,2);
85    i=find(deltau==0);
86    deltau(i)=-sigma;
87  %J(u_new) evaluation
88  %noisephi=cauchyrnd(0,noiseamp,1,2)
89  %noisephi=normrnd(0,noiseamp,1,2);
90   noisephi=zeros(2);
91   varphi=EOM(u_new,Vpi);
92  E=(E0_1.*(w0./w).*exp(-(sqrt((xvet-mu_x).^2+(yvet-mu_y).^2)').^2./w
       .^2)).*exp(-1j.*(k.*z-atan(z/z0))).*exp(-1j*k.*(sqrt((xvet-mu_x)
       .^2+(yvet-mu_y).^2)').^2./(2*R))*exp(1j*varphi(1))*exp(1j*
       noisephi(1))...
93       .*exp(1j.*(k*((nl-1).*(Delta01-(R1-sqrt(R1^2-xvet.^2-yvet.^2))+
            Delta02)+T_tot)')))...
94  +((E0_2.*(w0./w2).*exp(-(sqrt((xvet-mu_x2).^2+(yvet-mu_y2).^2)')
       .^2./w2.^2)).*exp(-1j.*(k.*z2-atan(z2/z0))).*exp(-1j*k.*(sqrt((
```

Appendix B (continued)

```
    xvet-mu_x2).^2+(yvet-mu_y).^2)').^2./(2*R2)))*exp(1j*varphi(2))*
    exp(1j*noisephi(1))...
95      .*exp(1j.*(k*((nl-1).*(Delta01-(R1-sqrt(R1^2-xvet.^2-yvet.^2))+
            Delta02)+T_tot)')));
96  i= find(abs(xvet)>xlens);
97  E(i,i)=0;
98  E=fftshift(fft2(fftshift((fftshift(ifft2(fftshift(E)))*Wx*Wx).*exp
    ((1j*2*pi/lambda).*(sqrt((1-(lambda.*fxvet').^2)-(lambda.*fyvet)
    .^2)*ff)))))/(Wx*Wx);
99  I_pert=(abs(E(pd_index,pd_index))).^2;
100 Px_pert=trapz(xvet(pd_index),I_pert);
101 P_pert=(trapz(yvet(pd_index),Px_pert));
102 R_1550_pert=1 ;% 1 A/W
103 Ipd_pert=P_pert*R_1550_pert;
104 J_new=Ipd_pert;
105 %Algorithm Would be Stopped Manually in Real Application
106 if o>30
107     flag=1;
108 end
109 J_old=J_new;
110 o=o+1
```

Appendix B (continued)

```
111 end
```

CITED LITERATURE

1. EdmundOptics: Beam quality and strehl ratio. `https://www.edmundoptics.com/knowledge-center/application-notes/lasers/beam-quality-and-strehl-ratio/`, 2020. [Online, accessed 01/10/20].

2. Naidoo, D., Litvin, I. A., and Forbes, A.: Brightness enhancement in a solid-state laser by mode transformation. Optica, 5(7):836–843, Jul 2018.

3. Donnelly, J. P., Huang, R. K., Walpole, J. N., Missaggia, L. J., Harris, C. T., Plant, J. J., Bailey, R. J., Mull, D. E., Goodhue, W. D., and Turner, G. W.: AlGaAs-InGaAs slab-coupled optical waveguide lasers. IEEE Journal of Quantum Electronics, 39(2):289–298, 2003.

4. Crump, P., Erbert, G., Wenzel, H., Frevert, C., Schultz, C. M., Hasler, K., Staske, R., Sumpf, B., Maaßdorf, A., Bugge, F., Knigge, S., and Tränkle, G.: Efficient high-power laser diodes. IEEE Journal of Selected Topics in Quantum Electronics, 19(4):1501211–1501211, 2013.

5. Fiebig, C., Blume, G., Kaspari, C., Feise, D., Fricke, J., Matalla, M., John, W., Wenzel, H., Paschke, K., and Erbert, G.: 12W high-brightness single-frequency dbr tapered diode laser. Electronics Letters, 44(21):1253–1255, 2008.

6. Tomm, J., Ziegler, M., Hempel, M., and Elsaesser, T.: Mechanisms and fast kinetics of the catastrophic optical damage (COD) in GaAs-based diode lasers. Laser Photonics Reviews, 5:422 – 441, 05 2011.

7. Beier, F., Hupel, C., Kuhn, S., Hein, S., Nold, J., Proske, F., Sattler, B., Liem, A., Jauregui, C., Limpert, J., Haarlammert, N., Schreiber, T., Eberhardt, R., and Tünnermann, A.: Single mode 4.3 kw output power from a diode-pumped yb-doped fiber amplifier. Opt. Express, 25(13):14892–14899, Jun 2017.

8. Yu, H.: Laser Diode Beam Spatial Combining. Doctoral dissertation, Politecnico di Torino, 2017.

9. Zheng, Y., Yang, Y., Wang, J., Hu, M., Liu, G., Zhao, X., Chen, X., Liu, K., Zhao, C., He, B., and Zhou, J.: 10.8 kw spectral beam combination of eight all-fiber superfluores-

CITED LITERATURE (continued)

cent sources and their dispersion compensation. Opt. Express, 24(11):12063–12071, May 2016.

10. Wirth, C., Schmidt, O., Tsybin, I., Schreiber, T., Eberhardt, R., Limpert, J., Tünnermann, A., Ludewigt, K., Gowin, M., ten Have, E., and Jung, M.: High average power spectral beam combining of four fiber amplifiers to 8.2 kw. Opt. Lett., 36(16):3118–3120, Aug 2011.

11. Jeux, F., Desfarges-Berthelemot, A., Kermène, V., Barthelemy, A., Sabourdy, D., and Montagne, J. E.: New design for passive coherent coupling of fiber lasers. In High-Power Lasers 2012: Technology and Systems, eds. H. Ackermann and W. L. Bohn, volume 8547, pages 129 – 137. International Society for Optics and Photonics, SPIE, 2012.

12. Schimmel, G., Doyen-Moldovan, I., Janicot, S., Hanna, M., Decker, J., Crump, P., Blume, G., Erbert, G., Georges, P., and Lucas-Leclin, G.: Rear-side resonator architecture for the passive coherent combining of high-brightness laser diodes. Opt. Lett., 41(5):950–953, Mar 2016.

13. Loftus, T. H., Thomas, A. M., Norsen, M., Minelly, J. D., Jones, P., Honea, E., Shakir, S. A., Hendow, S., Culver, W., Nelson, B., and Fitelson, M.: Four-channel, high power, passively phase locked fiber array. In Advanced Solid-State Photonics, page WA4. Optical Society of America, 2008.

14. McNaught, S. J., Asman, C. P., Injeyan, H., Jankevics, A., Johnson, A. M., Jones, G. C., Komine, H., Machan, J., Marmo, J., McClellan, M., Simpson, R., Sollee, J., Valley, M. M., Weber, M., and Weiss, S. B.: 100-kw coherently combined nd:yag mopa laser array. In Frontiers in Optics 2009/Laser Science XXV/Fall 2009 OSA Optics & Photonics Technical Digest, page FThD2. Optical Society of America, 2009.

15. Yu, C. X., Augst, S. J., Redmond, S. M., Goldizen, K. C., Murphy, D. V., Sanchez, A., and Fan, T. Y.: Coherent combining of a 4 kw, eight-element fiber amplifier array. Opt. Lett., 36(14):2686–2688, Jul 2011.

16. Goodno, G. D., Asman, C. P., Anderegg, J., Brosnan, S., Cheung, E. C., Hammons, D., Injeyan, H., Komine, H., Long, W. H., McClellan, M., McNaught, S. J., Redmond, S., Simpson, R., Sollee, J., Weber, M., Weiss, S. B., and Wickham, M.: Brightness-scaling potential of actively phase-locked solid-state laser arrays. IEEE Journal of Selected Topics in Quantum Electronics, 13(3):460–472, 2007.

CITED LITERATURE (continued)

17. Pullford, B.: LOCSET phase locking : operation, diagnostics, and applications. Doctoral dissertation, The University of New Mexico, Albuquerque, 2012.

18. Hanna, M., Guichard, F., Zaouter, Y., Papadopoulos, D. N., Druon, F., and Georges, P.: Coherent combination of ultrafast fiber amplifiers. Journal of Physics B: Atomic, Molecular and Optical Physics, 49(6):062004, February 2016.

19. Paschotta, R.: Electro optic modulators. `https://www.rp-photonics.com/electro_optic_modulators.html`, 2020. [Online, accessed 01/20/20].

20. Tao, Y.: Integrated Electro Optics Modulator. IntechOpen, 2019.

21. Thorlabs: Proposed approach for driving eo phase modulators. `https://www.thorlabs.com/newgrouppage9.cfm?objectgroup_id=3918`, 2020. [Online, accessed 01/25/20].

22. Brignon, A.: Choerent Laser Beam Combining. Wiley Online Library, 2013.

23. G. D. Goodno, e. a.: Active phase and polarization locking of a 1.4 kW fiber amplifier. Opt. Lett, 35(10):1542–1544, May 2010.

24. Fibercore: Mode field diameter(mfd). `https://www.fibercore.com/expertise/fiberpaedia/mode-field-diameter-mfd`, 2020. [Online, accessed 03/05/20].

25. Paschotta, R.: Field Guide To Laser. SPIE Press, 2008.

26. Thorlabs: Theoretical approximation of the output beam diameter. `https://www.thorlabs.com/newgrouppage9.cfm?objectgroup_id=2940`, 2020. [Online, accessed 01/26/20].

27. Bandres, M. A. and Gutiérrez-Vega, J. C.: Ince-gaussian beam. Opt. Lett, 29(10):144–146, January 2004.

28. Goodman, J.: Introduction to Fourier Optics 2nd edition. The McGraw-Hill Companies, inc., 1996.

29. EdmundOptics: 1550nm laser line coated plano-convex (pcx) lenses. `https://www.edmundoptics.com/f/1550nm-laser-line-coated-plano-convex-pcx-lenses/14309/`, 2020. [Online, accessed 02/08/20].

CITED LITERATURE (continued)

30. Chao, G., Wen, L., Yi, T., Hongmei, L., Jinbo, M., and Xinyang, L.: Experimental demonstration of using divergence cost-function in spgd algorithm for coherent beam combining with tip/tilt control. Optics express, 21:25045–55, October 2013.

31. Thorlabs: Ingaas free-space amplified photodetectors. `https://www.thorlabs.com/newgrouppage9.cfm?objectgroup_id=4&pn=PDA10CS2#10780`, 2020. [Online, accessed 02/15/20].

32. Anderegg, J., Brosnan, S., Cheung, E., Epp, P., Hammons, D., Komine, H., Weber, M., and Wickham, M.: Coherently coupled high-power fiber arrays. In Fiber Lasers III: Technology, Systems, and Applications, volume 6102, pages 202 – 206. SPIE, 2006.

33. Geng, C., Luo, W., Tan, Y., Liu, H., Mu, J., and Li, X.: Experimental demonstration of using divergence cost-function in spgd algorithm for coherent beam combining with tip/tilt control. Opt. Express, 21(21):25045–25055, October 2013.

34. Borghoff, J., Knudsen, L. R., , and Matusiewicz, K.: Hill climbing algorithms and trivium. In Selected Areas in Cryptography, pages 57–73. Springer, 2011.

35. Gosavi, A.: Simulation Based Optimization, Parametric Optimization Techniques and Reinforcement Learning, volume 55. Springer, 2014.

36. Song, Y., Chen, T., Wang, J., and Qiao, B.: Optimization of stochastic parallel gradient descent algorithm via power spectrum method. Applied Mathematics & Information Sciences, pages 325–332, 01 2016.

37. Spall, J. C.: Multivariate stochastic approximation using a simultaneous perturbation gradient approximation. IEEE Transactions on Automatic Control, 37(3):332–341, 1992.

38. Fu, Q., Pott, J.-U., Shen, F., Rao, C., and Li, X.: Stochastic parallel gradient descent optimization based on decoupling of the software and hardware. Optics Communications, 310(1):138–149, January 2014.

39. Piatrou, P. and Roggemann, M.: Beaconless stochastic parallel gradient descent laser beam control: numerical experiments. Appl. Opt., 46(27):6831–6842, Sep 2007.

CITED LITERATURE (continued)

40. Huang, Z. M., Liu, C. L., Li, J. F., and Zhang, D. Y.: A high-speed, high-efficiency phase controller for coherent beam combining based on SPGD algorithm. Quantum Electronics, 44(4):301–305, April 2014.

41. Liu, L., Vorontsov, M. A., Polnau, E., Weyrauch, T., and Beresnev, L. A.: Adaptive phase-locked fiber array with wavefront phase tip-tilt compensation using piezoelectric fiber positioners. In Atmospheric Optics: Models, Measurements, and Target-in-the-Loop Propagation, volume 6708, pages 169 – 180. SPIE, 2007.

42. Montoya, J., Augst, S. J., Creedon, K., Kansky, J., Fan, T. Y., and Sanchez-Rubio, A.: External cavity beam combining of 21 semiconductor lasers using spgd. Appl. Opt., 51(11):1724–1728, Apr 2012.

43. Wang, H., Kawahito, Y., Yoshida, R., Nakashima, Y., and Shiokawa, K.: Development of a high-power blue laser (445 nm) for material processing. Opt. Lett., 42(12):2251–2254, Jun 2017.

44. Bien Chann, R. H.: Scalable wavelength beam combining system and method, 2013. US Patent: US8559107B2.

45. Thorlabs: Visible transmission gratings. `https://www.thorlabs.de/newgrouppage9.cfm?objectgroup_id=1123`, 2020. [Online, accessed 04/05/20].

46. Nilse, L., Davies, H. J., and Adams, C. S.: Synchronous tuning of extended cavity diode lasers: the case for an optimum pivot point. Opto-Electronics Review, 38(3):548–553, 1999.

47. Mroziewicz, B.: External cavity wavelength tunable semiconductor lasers - a review. Opto-Electronics Review, 16(4):347 – 366, 2008.

VITA

NAME	Mattia Caffa
EDUCATION	
	Master of Science in "Electrical and Computer Engineering, University of Illinois at Chicago,May 2020 (expected), USA
	Master Degree in Electronics Engineering, Specialization in "Device and Technologies for ICT and Optoelectronics ",July 2020 (expected), Polytechnic of Turin, Italy
	Bachelor's Degree in Electronics Engineering, Oct 2018, Politecnico di Torino, Italy
LANGUAGE SKILLS	
Italian	Native speaker
English	2014-Cambridge English level 1 Certificate in ESOL international(First) : Grade B
	2019 - IELTS examination (7.0/9)
	A.Y. 2019 Fall semester of study abroad in Chicago, Illinois
	A.Y. 2018/2019. Lessons and exams attended exclusively in English
SCHOLARSHIPS	
Fall 2020	Italian scholarship for TOP-UIC students
TECHNICAL SKILLS	
Basic level	Python
Average level	Ansys HFSS
	Sentaurus TCAD
	Altium Designer
	MS Office
	Quartus
Advanced level	C and C++ programming
Advanced level	Matlab

VITA (continued)

WORK EXPERIENCE AND PROJECTS

2019	Design, implementation with Ansys HFSS, printing and testing at Andrew Lab of a 5.4 GHz antenna.
	Simulation of various electromagnetic scattering problems on Ansys HFSS.
2019	Simulation of semiconductor devices on Sentaurus TCAD
	Simulation of microwave circuits on MS office.
2018	Design, VHDL description , synthesis, simulation and testing on FPGA of finite state machines to solve different problems.
2018	Internship at SEICA Spa, Strambino, Italy: design and implementation, using Altium Designer, of a PCB transceiver based on S2-LP module from STmicroelectronics
	Various projects with the microcontroller of an NPX Freescale Tower.